

Received Date : 12-Apr-2016

Revised Date : 09-Jul-2016

Accepted Date : 09-Aug-2016

Article type : Original Article

## **Oligocene-Miocene Great Lakes in the India-Asia Collision Zone**

Peter G. DeCelles\*<sup>1</sup>, Isla S. Castañeda<sup>2</sup>, Barbara Carrapa<sup>1</sup>,

Juan Liu<sup>3</sup>, Jay Quade<sup>1</sup>, Ryan Leary<sup>1</sup>, and Liyun Zhang<sup>4, 5</sup>

<sup>1</sup>Department of Geosciences, University of Arizona, Tucson AZ 85721 USA.

<sup>2</sup>Department of Geosciences, University of Massachusetts Amherst, Amherst, MA 01003 USA.

<sup>3</sup>Department of Biological Sciences, University of Alberta, Edmonton, AB T6G 2E9, Canada.

<sup>4</sup>Key Laboratory of Continental Collision and Plateau Uplift, Institute of Tibetan Plateau Research, Chinese Academy of Sciences, Beijing 100101, China.

<sup>5</sup>CAS Center for Excellence in Tibetan Plateau Earth Sciences, Beijing 100101, China

This article has been accepted for publication and undergone full peer review but has not been through the copyediting, typesetting, pagination and proofreading process, which may lead to differences between this version and the Version of Record. Please cite this article as doi: 10.1111/bre.12217

This article is protected by copyright. All rights reserved.

Running Head: Great Lakes in the India-Asia Collision Zone

## ABSTRACT

The Himalayan-Tibetan Plateau is Earth's highest topographic feature, and formed largely during Cenozoic time as India collided with and subducted beneath southern Asia. The >1300 km long, late Oligocene-early Miocene Kailas basin formed within the collisional suture zone more than 35 Ma after the onset of collision, and provides a detailed picture of surface environments, processes, and possible geodynamic mechanisms operating within the suture zone during the ongoing convergence of India and Asia. We present new geochronological, sedimentological, organic geochemical, and palaeontological data from a previously undocumented 400 km long portion of the Kailas basin. The new data demonstrate that this part of the basin was partly occupied by large, deep, probably meromictic lakes surrounded by coal-forming swamps. Lacustrine facies include coarse- and fine-grained turbidites, profundal black shales, and marginal Gilbert-type deltas. Organic geochemical temperature proxies suggest that palaeolake water was warmer than 25°C, and cyprinid fish fossils indicate an ecology capable of supporting large fish. Our findings demonstrate a brief period of low elevation in the suture zone during Oligocene-Miocene time (26-21 Ma) and call for a geodynamic mechanism capable of producing a long (>1000 km) and narrow basin along the southern edge of the upper, Asian plate, long after the onset of intercontinental collision. Kailas basin deposits presently are exposed at elevations

>6000 m, requiring dramatic elevation gain in the region after Kailas deposition, without strongly shortening the upper crust. Episodic Indian slab rollback, followed by break-off and subsequent renewal of flat-slab subduction, can account for features of the Kailas basin.

## INTRODUCTION

Palaeocene collision of continental India and southern Asia (Garzanti et al., 1987; Wu et al., 2014; DeCelles et al., 2014; Orme et al., 2014; Hu et al., 2015) followed by ongoing northward movement of India has produced the thickest crust and highest mountains on Earth—the Himalayan-Tibetan orogen (Dewey et al., 1988) (Fig. 1a). The timing and mechanisms by which Tibet has risen from below sea-level during mid-Cretaceous time (Leier et al., 2007a, 2007b) to greater than 5000 m at present are not well known, partly because palaeoaltimetry proxies only recently have begun to illuminate the history of elevation gain (Garzanti et al., 2000; Currie et al., 2005, 2016; Rowley & Currie, 2006; DeCelles et al., 2007; Saylor et al., 2009; Quade et al., 2011; Zhuang et al., 2014; Hoke et al., 2014; Huntington et al., 2015). Lake deposits worldwide are an important archive of palaeoclimatic and palaeoaltimetric information (Cohen, 2003). Tibetan lakes formed during the Neogene are recorded by carbonate-rich, fossil-poor deposits that accumulated at very high elevation (e.g., DeCelles et al., 2007; Saylor et al., 2009; Quade et al., 2011), much like the highly evaporative lakes of modern Tibet (Zhang et al., 2013). On the other hand, the Oligocene-early Miocene Kailas basin in southern Tibet formed in a more productive environment, as indicated by the presence of fossiliferous, organic-rich, freshwater lake deposits, coal, and related alluvial and fluvial deposits (DeCelles et al., 2011). The Kailas basin is puzzling because it formed more than 35 Ma after the onset of intercontinental

collision along the southern fringe of the upper tectonic plate only a few km north of the India-Asia suture zone, in a region where crustal thickening, elevation gain, and deep erosion are expected, rather than accumulation of a thick succession of sediments. Most intriguing is the presence of thick, lacustrine black shale and coal in the Kailas basin; these lithofacies are not expected in high-elevation settings. Whereas peat-forming mires exist in high-elevation settings (e.g., Large et al., 2009; Maldonado Fonkén, 2014), significant accumulations of coal are not documented in known high-elevation basins in the stratigraphic record (e.g., McCabe, 1984). Attempts to reconstruct palaeoelevation in Kailas basin lacustrine deposits using stable isotope methods (Quade et al., 2011) are stymied by deep burial diagenesis that has raised formation temperatures above the closure temperature of apatite fission tracks (Carrapa et al., 2014) and recrystallized calcitic fossils. Our previous work on the Kailas basin was restricted to the Kailas Range in southwestern Tibet (DeCelles et al., 2011). That work documented the stratigraphy and geochronology of the Kailas Formation, but left unanswered many questions regarding the palaeoenvironment of deposition because of uncertainty in the palaeoelevation and palaeotemperature of the basin. Here we report new data from physical sedimentology, organic geochemistry, palaeontology, and detrital zircon geochronology of the Kailas basin fill along a previously undocumented 400 km stretch of the basin to reconstruct its palaeoenvironment, age, and probable palaeoelevation during deposition. Of special interest are the lacustrine facies in the Kailas Formation, which have not been studied in any detail.

## THE KAILAS BASIN

The Kailas basin is represented by a narrow but regionally extensive belt of outcrops of the Kailas Formation (Gansser, 1964; Murphy & Yin, 2003; DeCelles et al., 2011) (Fig. 1a, b). The Kailas Formation is up to 4 km thick (Gansser, 1964) and forms some of the highest (>6000 m) peaks of the Gangdese Shan (or Transhimalaya), including culturally sacred Mount Kailas in southwestern Tibet. The Kailas Formation was deposited on an irregular surface incised into Cretaceous-Eocene rocks of the Gangdese magmatic arc, which formed during subduction of Indian plate oceanic and continental lithosphere beneath southern Asia prior to and during the collision (e.g., Schärer et al., 1984; Kapp et al., 2005; Chung et al., 2005). This unconformity surface has been tilted (after deposition of the Kailas Formation) 10-40° southward along most of its regional extent, although locally the Kailas Formation is considerably more deformed (Wang et al., 2015; Leary et al., 2016a). The southern margin of the Kailas Formation outcrop belt is marked by folds and thrust faults of the Great Counter Thrust system, which accommodated northward relative displacement of ophiolites and Cretaceous-lower Eocene Xigaze forearc basin deposits against the Kailas Formation (Gansser, 1964; Murphy & Yin, 2003; Orme et al., 2014) (Fig. 1b).

## METHODS

### Fieldwork

Stratigraphic sections were measured with a tape measure and Jacob's staff at a bed-by-bed scale, and recorded on 1:100 section logs. Samples of tuffaceous layers, sandstone, and organic-rich shale were collected for geochronology and organic

geochemistry. Shale samples were collected by digging at least 50 cm below the surface and then gathering chips of fresh rock with a hammer pick.

### **Organic Geochemistry**

The organic geochemistry of nine shale samples of the Kailas Formation was examined (Table 1). For each sample, the outer layer of material was removed and subsequently 42-180 g was homogenized with a mortar and pestle. Samples were extracted with 9:1 dichloromethane (DCM)/methanol (v/v) using an Accelerated Solvent Extractor (ASE 200) to obtain a total lipid extract (TLE). Due to the large sample size, multiple ASE cells were packed for each sample and the resulting TLEs combined. Base hydrolysis was performed on the TLE by refluxing each sample with a 1N KOH solution for an hour, adjusting the pH to 5 with a 2N HCl/MeOH solution and then washing the MeOH/H<sub>2</sub>O layer 3x with DCM. Samples were next put through a sodium sulfate column to remove water. Each sample was subsequently separated into apolar, ketone and polar fractions via alumina oxide pipette column chromatography using solvent mixtures of 9:1 hexane/DCM (v/v), 1:1 hexane/DCM (v/v), and 1:1 DCM/methanol (v/v), respectively. The polar fractions were next split and half were derivatized to trimethylsilyl-ethers in 50  $\mu$ L bistrimethylsilyltrifluoroacetamide (BSTFA) and 50  $\mu$ L acetonitrile at 70 °C for 30 minutes immediately prior to analysis.

The apolar, ketone and derivatized polar fractions were analyzed on a Hewlett Packard 6890 series gas chromatograph – mass spectrometer (GC-MS) using an HP-5 column (60 m x 0.25 mm x 0.25  $\mu$ m). The GC-MS oven temperature program initiated at 70 °C, increased at a rate of 10 °C min<sup>-1</sup> to 130 °C and then increased at a rate of 4 °C min<sup>-1</sup> to 320 °C, and held for 20 min. Mass scans were made over the interval from 50 to 600 m/z.

Compound identification was achieved by interpretation of characteristic mass spectra fragmentation patterns, GC relative retention times, and by comparison with the literature.

The underivatized polar splits were dissolved in a mixture of 99:1(v/v) hexane/isopropanol and filtered through a 0.45  $\mu\text{m}$  PTFE filter before being analyzed by high performance liquid chromatography mass-spectrometry (HPLC-MS) for glycerol dialkyl glycerol tetraethers (GDGTs) following the methods described by Hopmans et al., (2000) and modified slightly by Schouten et al. (2007). Samples were initially analyzed on an Agilent 1260 series LC/MSD using a Prevail Cyano column (150 mm x 2.1 mm, 3  $\mu\text{m}$ ) and 99:1 hexane:propanol (vol:vol) as the eluent. After 5 minutes, the eluent increased by a linear gradient up to 1.8 % isopropanol (vol) over the next 45 min at a flow rate of 0.2 mL min<sup>-1</sup>. Scanning was performed in single ion monitoring (SIM) mode.

## Geochronology

Seven samples of medium- to coarse-grained sandstone were processed by standard methods for retrieving dense minerals, and detrital zircon grains were separated from these concentrates using heavy liquids. Zircons were mounted in epoxy, polished, and analyzed for U-Pb ages by laser ablation multicollector inductively coupled plasma mass spectrometry (LA-MC-ICPMS) at the University of Arizona LaserChron Center. The methods employed are described in Gehrels et al. (2008). A total of 656 detrital zircon grains produced data of sufficient precision for geochronological interpretation. Analyses that yielded isotopic data of acceptable discordance, in-run fractionation, and precision are listed in Supporting Information Table S1. Because <sup>206</sup>Pb/<sup>238</sup>U ages are generally more precise for younger ages

whereas  $^{206}\text{Pb}/^{207}\text{Pb}$  ages are more precise for older ages, we report  $^{206}\text{Pb}/^{238}\text{U}$  ages up to 1000 Ma and  $^{206}\text{Pb}/^{207}\text{Pb}$  ages if the  $^{206}\text{Pb}/^{238}\text{U}$  ages are >1000 Ma (Gehrels et al., 2008). All detrital ages are listed in Supporting Information Table S1.

We also collected and processed seven samples for U-Pb geochronology from tuffaceous layers at various locations and levels of the Kailas Formation. Clear euhedral zircons were picked, mounted in epoxy, polished, and analyzed for U-Pb ages by LA-MC-ICPMS at the LaserChron Center. Analytical data for these samples are provided in Supporting Information Table S2.

## **SEDIMENTOLOGY OF THE KAILAS FORMATION**

The sedimentology of the Kailas Formation in its type area (the Kailas Range of southwestern Tibet) was described by DeCelles et al. (2011). However, new measured sections (Figs. 2-5) provide information about the previously poorly documented southern and axial parts of the Kailas basin fill, which are the foci of this paper. All lithofacies documented in the Kailas Formation in this work are listed in Table 2. In most stratigraphic sections that we have measured (Fig. 1a) the Kailas Formation is divisible into a lower conglomeratic member, a middle shale and sandstone member, and an upper sandstone and conglomerate member. The formation is commonly folded into an asymmetric syncline with an axial surface dipping steeply southward near the Great Counter thrust (Fig. 1b). The distribution of lithofacies is also asymmetric in north-south cross-section: The lower conglomerate member is thickest (up to 800 m thick) and coarsest in the northern part of the basin where it rests upon Gangdese arc rocks; the central sector of the basin is



dominated by shale and tabular sandstone beds; and the southern portion of the basin contains interbedded conglomeratic and fine-grained material. Overall the stratigraphy defines a coarse-fine-coarse sandwich (Figs. 1b, 2-5).

### **Lithofacies Descriptions**

The lower conglomerate member consists of poorly sorted, disorganized boulder- to cobble-conglomerate (Fig. 6d) interbedded with better-organized, horizontally stratified and imbricated cobble-conglomerate. These lithofacies were interpreted by DeCelles et al. (2011) as, respectively, debris-flow and stream-flow deposits that accumulated in proximal alluvial fan environments. These coarse-grained lithofacies grade southward into sandy fluvial braidplain lithofacies (DeCelles et al., 2011).

The axial fine-grained part of the basin fill is composed of 220-500 m thick (Figs. 2, 4) successions of black and dark gray, organic-rich, laminated clay-shale (Figs. 7a, b). Interbedded within thick shale successions are sequences of upward-thickening and -coarsening sandstone beds, which were interpreted by DeCelles et al. (2011) as progradational deltaic parasequences grading upward from distal, profundal, laminated shale (Fig. 7b) to proximal fluvial and deltaic mouth-bar deposits. These parasequences are up to 100 m thick.

Not observed by DeCelles et al. (2011), but also interbedded within thick shale successions, are tabular sandstone beds, typically 10-40 cm thick, composed of upward fining, coarse- to very fine-grained sandstone (Fig. 7c). Most of these beds have a structureless lower part, a parallel-laminated middle part, and a thin upper layer containing

small asymmetrical ripple cross-laminations. Structureless, inversely or normally graded beds are common (Fig. 2, section 1JV). Most of these sandstone beds have basal sole marks (flute and groove casts, prod and bounce marks) (Figs. 7f, g). These beds occur as stacked successions a few m to >10 m thick (Fig. 7c), in isolated lenticular bodies up to 10 m thick with erosional basal surfaces and flat tops (Fig. 7a), and as interbeds within coarser conglomeratic parts of the section. Slump folds are present in some of these sandstone beds (Fig. 7e).

The southern part of the basin fill contains clast- and matrix-supported conglomerate beds intercalated with finer-grained lithofacies (Fig. 2). Matrix-supported conglomerates have well-sorted, fine- to coarse-grained sandstone matrix and well-rounded clasts that commonly have long axes streamlined parallel to palaeoflow direction (a-axis imbrication; Figs. 6a, 7d). Most conglomerate beds have sharp erosional basal surfaces, but deep irregular scours are rare. Conglomerate beds are capped by 10-30 cm thick layers of massive, laminated, or rippled sandstone. In section 3JV (265-305 m levels), steeply inclined mega-foreset bedding composed of conglomeratic layers dips 25° relative to master bedding (Fig. 6c).

### **Lithofacies Interpretations**

The conglomeratic lithofacies typical of the northern margin of Kailas basin (in the lower conglomerate member) are characteristic of proximal alluvial fan depositional systems (for a more in-depth discussion, see DeCelles et al., 2011). As mentioned above, our

focus in this paper is on the finer-grained facies in the middle part of the basin and on the fringing coarse-grained facies along the southern edge of the basin.

Sandstone beds in the middle part of the Kailas Formation exhibit characteristics of deposition by dilute turbidity currents, including tabular geometry, basal erosional surfaces with sole marks, incomplete (divisions a-c) Bouma sequences (Bouma, 1962; Walton, 1967; Mutti, 1992), and abrupt alternation of grain-size due to pulsing flow and highly unsteady depositional events (Mutti, 1992). The inversely graded layers of granular to very coarse-grained sandstone resemble density-modified grainflows, deposited from high-density turbidity flows under conditions of extreme sediment fallout (Lowe, 1982). Conglomerate beds also exhibit features typical of coarse-grained turbidites (Lowe, 1982; Mutti, 1992; Talling et al., 2012), subaqueous debris flows (Nemec & Steel, 1984), and concentrated density flows (Mulder & Alexander, 2001), including sandy matrix support (Fig. 6a), long-axis clast imbrication (Fig. 7d), and abrupt alternation between conglomerate and shale lithofacies. Progradational profundal to upper shoreface sequences up to 100 m thick suggest water at least that deep, and much deeper once the sections are decompacted. The mega-foreset bedsets in the southern part of the basin fill (Fig. 6c) represent steep subaqueous (Gilbert-type) delta clinoforms (e.g., Colella, 1988; Dorsey et al., 1995; Johnson et al., 1995). The sedimentological evidence for deep-water sedimentation, organic-rich, laminated but not varved profundal deposits, and absence of evaporitic facies suggests that the Kailas lakes were perennial, deep, fresh-water, and probably meromictic.

Combined with our previous work on the Kailas Formation in southwestern Tibet, the new data lead to a basin model in which the earliest part of the basin fill is dominated by coarse-grained alluvial fan deposits shed from the Gangdese magmatic arc. A major

lacustrine transgression inundated the basin during deposition of the middle fine-grained member, and coarse- and fine-grained sediment-gravity flows supplied sediment to the medial part of the basin while deltas, fan-deltas, and coal-forming swamps occupied the fringes of the basin (Fig. 8). During the latter part of the basin history, deltaic and fluvial conglomeratic and sandy deposits prograded across the basin as it filled to subaerial conditions. These stratigraphic and lithofacies patterns are consistent with models for extensional continental rift basins, both ancient and modern (e.g., Lambiase, 1990; Schlische, 1992; Johnson et al., 1995; Gawthorpe & Leeder, 2000).

## GEOCHRONOLOGY

The Kailas Formation contains abundant volcanogenic material, including occasional lava flows and ash-flow tuffs, as well as abundant near-depositional-age detrital zircons. Uranium-Lead (U-Pb) ages from detrital and igneous zircons (DeCelles et al., 2011) and  $^{40}\text{Ar}/^{39}\text{Ar}$  ages from phlogopite crystals in lava flows (Carrapa et al., 2014) indicate that the Kailas Formation in the Mt. Kailas area was deposited between 26 and 23 Ma. Here we report 656 new U-Pb detrital zircon ages from seven sandstone samples (Fig. 9), along with new U-Pb zircon ages from seven tuffaceous layers (Fig. 10). Analyses that produced ages equal to or younger than 200 Ma are plotted on relative age-probability diagrams (Fig. 9). Age peaks on these diagrams are considered robust if defined by several analyses. Combined with the previously reported data, the new results extend the range of Kailas Formation deposition to ca. 21 Ma and demonstrate that the unit is chronologically consistent along strike for at least 500 km. The younger-than-200 Ma detrital zircon populations (Fig. 9) are dominated by ages in the 48-51 Ma and 22-25 Ma ranges. Both of

these time intervals were characterized by igneous activity in the southern Lhasa terrane:

The Eocene episode coincides with a strong pulse of activity in the Gangdese arc, and the Oligo-Miocene episode was coeval with Kailas deposition and emplacement of adakitic and high-K magmas in the suture zone (e.g., Chung et al., 2005).

The available geochronological data suggest that the entire Kailas Formation was deposited over a period of no longer than ~5 Myr, implying sediment accumulation rates on the order of 1 mm/yr. Apatite fission track and zircon (U-Th)/He ages from the Kailas Formation and underlying Gangdese arc rocks require temperatures of 120-230°C during post-depositional burial heating after ca. 21 Ma, suggesting that the total thickness of the Kailas basin could have been 6 km (Carrapa et al., 2014). Rapid cooling commenced at ca. 17 Ma as a result of basin incision and sediment evacuation (Carrapa et al., 2014).

## **PALAEONTOLOGY OF THE KAILAS FORMATION**

The Kailas Formation contains aquatic vertebrate and invertebrate fossils, plant fossils, and coal. Vertebrate fossil materials mainly represent turtles and fish. Palynological study indicates the presence of abundant, thermally mature, amorphous kerogen, and sparse pollen taxa including Elm and equatorial fern floras. Pollen from temperate or high elevation boreal species has not been found (DeCelles et al., 2011).

Disarticulated bones of freshwater fossil fish in the Kailas Formation are concentrated in pebbly lags along transgressive surfaces at the tops of thick lacustrine shoreface parasequences. Closely resembling the modern fish fauna of Tibet (Wu & Wu, 1992), the Kailas fish fauna is characterized by low species diversity and represented by

cyprinids (Order Cypriniformes, Family Cyprinidae; Fig 11). The dominant modern fish on the Tibetan Plateau are schizothoracines (Cyprinidae, Subfamily Schizothorinae; known as snow trout) endemic to the plateau and its surrounding areas, and probably evolved from another cyprinid subfamily Barbinae (*sensu stricto*) adapting to environmental changes that accompanied the development of the plateau. Limited fossil records of cyprinids from the plateau span early Oligocene to Pleistocene time. In rocks older than late Oligocene, only primitive barbines have been found (Chen & Liu, 2007; Wang & Wu, 2014), whereas moderately specialized (Wu & Chen, 1980; Chang et al., 2008) and highly specialized schizothoracines (Wang & Chang, 2010) occur from the Pliocene to the Pleistocene. The Kailas fish fauna represents the only known fish remains of Tibetan cyprinids during the late Oligocene-early Miocene, a time that witnessed the early evolution of schizothoracines.

The Kailas cyprinid discovery includes spines of the last unbranched dorsal fin ray with serrations (also possibly from the anal fin, but less likely because the last unbranched anal fin ray with serrations is found only in the Tribe Cyprinini *sensu* Yang et al., 2010; Fig. 11a), vertebral centra (Fig. 11b, eight annuli), an incomplete pharyngeal bone (Fig. 11c), and numerous fragmentary bones. The spine with posterior serration (Fig. 11a) of the dorsal fin is commonly seen in certain cyprinids, including some barbines and all schizothoracines (secondarily reduced in some adults). It is an anti-predator weapon for small or juvenile schizothoracines to prevent being swallowed by large piscivorous schizothoracines (Tsao & Wu, 1962). Based on the ratio of dorsal spine length to standard length of *Plesioschizothorax macrocephalus* (20—32 mm/287—340 mm) and *Hsianwenia wui* (IVPP V 15244, 43.3 mm/445 mm) calculated from published data (Wu & Chen, 1980; Chang et al., 2008), the estimated original standard length of the fish IVPP V 20855.1 to which the spine (length >45

mm) belonged is more than 450 mm, which is comparable to the maximum size of modern Tibetan schizothoracines. The palaeontological evidence, including disarticulated bones, large reconstructed size of IVPP V 20855.1, and longevity of IVPP V 20855.2, demonstrate that the Kailas lacustrine facies were deposited in large freshwater bodies capable of sustaining an ecological system able to support large fish.

## ORGANIC GEOCHEMISTRY OF KAILAS FORMATION SHALES

The organic geochemistry of nine samples from the Kailas Formation was examined to investigate the main sources of organic matter (see Methods). Three samples were found to be thermally mature, two samples did not yield any detectable biomarkers, but four were unaltered and yielded a suite of compounds useful for environmental reconstruction (Table 1). The thermally immature samples contained short- and long-chain *n*-alkanes and *n*-alkanols, attributed to sources from algae or bacteria and higher land plants, respectively. These samples yielded similar biomarker distributions with the apolar fractions dominated by short-chain C<sub>16</sub>, C<sub>17</sub> and C<sub>18</sub> *n*-alkanes and *n*-alkenes, and the polar fractions by the C<sub>18</sub> *n*-alkanol. The polar fractions also contained low concentrations of sterols and stanols, including cholesterol (cholest-5-en-3 $\beta$ -ol),  $\beta$ -sitosterol (24-ethylcholesta-5-en-3 $\beta$ -ol), and dinostanol (4,23,24-trimethylcholestan-3 $\beta$ -ol). Cholesterol is produced by eukaryotes but is common in microalgae;  $\beta$ -sitosterol is attributed to sources from both microalgae and higher plants; and dinostanol is produced by dinoflagellates and some diatom species (Volkman, 2003). The predominance of short- over long-chain *n*-alkanes, in addition to the presence of sterols commonly associated with microalgae, suggests a dominant aquatic (lacustrine) organic matter source.

Four Kailas Formation samples also contained isoprenoid and branched glycerol dialkyl glycerol tetraethers (GDGTs), with two having abundances sufficient for palaeotemperature reconstruction using the TEX<sub>86</sub> (Schouten et al., 2001) and MBT/CBT Indices (Weijers et al., 2007; Peterse et al., 2012) (Tables 3 and 4). TEX<sub>86</sub> and MBT values can range from 0 to 1, with higher values associated with higher temperatures. Kailas Formation samples have TEX<sub>86</sub> values of 0.73-0.80 and MBT/CBT values of 0.65-0.78. Although both indices have been calibrated to lake surface temperature, we caution against absolute temperature reconstruction because multiple calibrations exist for both proxies and, as discussed below, it is not clear which are the most appropriate to apply (e.g., Tables 3 and 4).

The TEX<sub>86</sub> temperature proxy is based on isoprenoid GDGTs produced by Thaumarchaeota and members of the domain Archaea (Schouten et al., 2002). This technique has been widely applied to marine sediment to reconstruct sea surface temperature (SST) and also to some lacustrine sediments to reconstruct lake surface temperature (LST) (e.g. Powers et al., 2010; Castañeda and Schouten, 2011 and references therein). Several calibrations to SST or LST exist for the TEX<sub>86</sub> proxy. Applying the LST calibration of Powers et al. (2010) yields temperatures in the range of 26-30°C while the marine SST calibrations of Schouten et al. (2002) and Kim et al. (2010) yield temperatures of 30-34°C and 29-32°C, respectively (Table 3). In marine samples TEX<sub>86</sub> temperatures can be influenced by inputs of terrestrially derived isoprenoid GDGTs from soils and this influence can be assessed using the Branched and Isoprenoid Tetraether (BIT) Index (Hopmans et al., 2004). However, in lakes, the BIT Index may not be informative as branched GDGTs (hereafter brGDGTs) are also produced *in situ* (e.g. Tierney and Russell, 2009; Schoon et al.,



2013; Buckles et al., 2014; Loomis et al., 2014); thus, high BIT values of Kailas samples do not necessarily indicate predominately terrestrial inputs of GDGTs. Importantly, we note that regardless of the calibration applied, the distribution of isoprenoid GDGTs in these samples is characteristic of high temperature conditions and resembles other samples from tropical locations (Fig. 12).

Another temperature proxy is provided by the Methylation and Cyclization Ratios of Branched Tetraethers (MBT/CBT) (Weijers et al., 2007). The MBT/CBT index was first developed as a proxy for mean annual soil temperature, which is generally similar to mean annual air temperature (MAAT). This technique was developed based on observations that the cyclization ratio of branched tetraethers (CBT) is related to soil pH whereas the degree of methylation of the brGDGT structure (MBT) is related mainly to temperature and to a lesser extent to pH (Weijers et al., 2007). Temperature can be derived by correcting MBT values for the influence of pH using CBT (Weijers et al., 2007). MBT/CBT is calibrated to MAAT using a set of globally distributed soil samples (Weijers et al., 2007), and was later updated by Peterse et al. (2012) to include additional sites while eliminating two of the brGDGTs that are often missing or present in extremely low concentrations in many soils. More recently, improvements in chromatography (de Jonge et al., 2014; Hopmans et al., 2016) showed that 6-methyl brGDGTs co-elute with 5-methyl brGDGTs and that the perceived dependence of MBT on pH was an artifact of the incomplete separation of the 5- and 6-methyl brGDGTs (de Jonge et al., 2014). Although we analyzed the Kailas samples using the original method of Weijers et al. (2007), and therefore note that MBT and CBT values reported here may be affected by co-elution of brGDGT isomers, we note that TEX<sub>86</sub> values remain the same whether the original or newer method is applied.

After the initial discovery of brGDGTs in soils, subsequent research revealed that brGDGTs are abundant in the water columns and sediments of lakes and also found that these compounds are produced *in situ* in lakes, most likely in the surface waters (Tierney and Russell, 2009; Schoon et al., 2013; Buckles et al., 2014; Loomis et al., 2014). A number of researchers have developed lacustrine calibrations relating either MBT/CBT or fractional abundances of brGDGTs in lake surface sediments to temperature (e.g., Tierney et al., 2010; Sun et al., 2011; Pearson et al., 2011; Loomis et al. 2012). Many of the existing lacustrine calibrations are regional and are based on a relatively small sample set. Applying several soil and lacustrine MBT/CBT calibrations to the Kailas Formation shale samples yields a wide range of reconstructed temperatures (Table 4). If we consider the extremes, the lacustrine calibration of Pearson et al. (2011) yields the lowest temperatures of 19-20°C whereas the lacustrine calibration of Tierney et al. (2010), which is based on African lakes, yields temperatures of 36-39°C. Although it is impossible to know whether the brGDGTs in Kailas shales were produced mainly within the water column of the palaeolake or from soils within its watershed, and thus it is not clear which calibration to apply, all calibrations suggest high temperatures that support the TEX<sub>86</sub> temperature estimates. Akin to the isoprenoid GDGT distributions, the brGDGT distributions of the Kailas Formation samples resemble those from tropical soils or lakes.

To summarize, despite uncertainties associated with calibration to absolute temperature, Kailas Formation samples are characterized by isoprenoid and brGDGT distributions indicative of deposition under warm water conditions (Fig. 12). Considering that the maximum summer water temperature of modern Tibetan Plateau lakes at 4220-4450 m elevation is around 16°C (Wang et al., 2014), this would translate to a TEX<sub>86</sub> value of

0.55, using the lacustrine calibration (Powers et al., 2010). Thus, TEX<sub>86</sub> values of 0.73-0.80 suggest deposition under significantly warmer temperatures, and probably lower elevation, than at present. Considering multiple TEX<sub>86</sub> and MBT/CBT calibrations (Tables 3 and 4) and applying empirically derived lapse rate equations (Quade et al., 2013; Huntington et al., 2015) to warm-season average lake water temperatures of ~20-35°C yields palaeoelevations of the lakes between 754 m and 3360 m above sea level. The high TEX<sub>86</sub> and MBT/CBT values favor the higher temperatures and imply that the lower end of this elevation range is more likely. We note that Liu et al. (2013) proposed a relationship between TEX<sub>86</sub> of soils and altitude in the northeastern Tibetan Plateau near Lake Qinghai, due to altitude-dependent temperature. However, these authors also observed that soils surrounding Lake Qinghai have significantly different TEX<sub>86</sub> values from those of the lake sediments. Thus their reported relationship between soil TEX<sub>86</sub> and altitude may not be appropriate for the lacustrine Kailas samples. Nevertheless, applying their equation yields altitudes of approximately 2700-3200 m. We stress that these palaeoelevation estimates are highly speculative.

## **DISCUSSION**

### **Palaeoenvironments and Palaeoelevation**

The combination of sedimentologic, palaeontologic, and organic geochemical data suggests that Kailas basin was occupied by large, deep, warm-water lakes. Although modern Tibet contains numerous large lakes, they differ dramatically from those in which the lacustrine facies of the Kailas Formation accumulated. Mean annual temperature over most

of the Tibetan Plateau is less than 0°C (Kropáček, et al., 2013), and Tibetan lakes have temperatures ranging between about 0°C and 15°C depending on season and depth of measurement; most are covered by ice and snow for months each year (Wang et al., 2014; Zhang et al., 2014). Confined within a north-trending rift, Tangri Yum Co (Fig. 1), with a depth of 230 m, is Tibet's deepest lake (Wang et al., 2010; Akita et al., 2015). Other large Tibetan lakes not located in rifts (e.g., Nam Co, Selin Co) are less than 100 m deep (Zhang et al., 2013). Organic-rich, fine-grained sediment is present in some Tibetan large lakes, but thick accumulations of black, laminated clay-rich sediment are not present in existing cores (Mügler, et al. 2010; Long et al., 2014). Similarly, palaeolakes in other late Oligocene–Pliocene basins of central and southern Tibet did not accumulate coal and thick black shale (Garzione et al., 2000; DeCelles et al., 2007; Saylor et al., 2009); Kailas basin is unique in this respect. All of these other basins contain lithofacies typical of shallow water and high evaporation rates, and are shown by stable isotope palaeoaltimetry studies to have formed at high elevations (>4000 m; Garzione et al., 2000; Currie et al., 2005, 2016; Rowley & Currie, 2006; DeCelles et al., 2007; Saylor et al., 2009; Quade et al., 2011; Zhuang et al., 2014; Huntington et al., 2015). Unfortunately, the lacustrine part of the Kailas Formation is largely thermally mature (>120 °C; Carrapa et al., 2014) and generally lacks carbonate that could be used for stable isotope palaeoaltimetry. Although leaf waxes were recovered in small quantities from our samples, they were not abundant enough for deuterium isotope analysis. Such data, in any case, might be compromised by evaporative enrichment of  $\delta^{18}\text{O}$  values or by diagenetic alteration (Huntington et al., 2015). Carbon and O isotope data from locally occurring palaeosol carbonate in the uppermost part of the Kailas Formation suggest very high palaeoelevation ( $4500 \pm 500$  m) but also more humid palaeoclimate (DeCelles et al., 2011), consistent with a warmer, largely ice-free world during the early Miocene.

(Shackleton and Kennett, 1975; Zachos et al., 1994; Bowen and Wilkinson, 2002). Together with the lithofacies data presented here, this implies that the Kailas basin evolved abruptly (probably within 1-2 Myr) from a warm, moist, low-elevation basin to one that was high and dry, like other middle Cenozoic Tibetan basins. Soon thereafter, the basin was rapidly incised (Carrapa et al., 2014).

Temperature differences between today and the early Miocene should be considered in our palaeoelevation reconstruction. Globally, modern climate is cooler than early Miocene climate, but most of that temperature difference is at high latitudes, where the surface ocean and possibly air temperature was as much as 6-7 °C warmer during the early Miocene (Lear et al., 2001; Zachos et al., 1994). In contrast, pole to equator temperature gradients were much lower during early to mid-Cenozoic, and most evidence points to little difference between Holocene and early Miocene ocean surface temperatures at low latitudes (Savin et al., 1985; Zachos, 1994). The Kailas Formation was deposited at low latitudes (ca. 20°N; Lippert et al., 2014). We assume that air temperature at these subtropical latitudes changed little over the last 25 Ma and make no “climate” correction to our mean paleoelevation estimates, but suggest that  $\pm 500$  m ( $\pm 2-3^{\circ}\text{C}$ ) of uncertainty be attached to our estimates to reflect possible minor temperature differences.

Our palaeogeographic reconstruction of Kailas basin as a low-elevation fluvial-lacustrine depocenter along the axis of the India-Asia suture zone raises additional questions about moisture transport paths and the palaeogeography of the Himalayan thrust belt to the south. Water in quantities sufficient to sustain large lakes is available in the modern Yarlung Tsangpo drainage system, provided the system is partly or wholly hydrographically closed. Thus, our reconstruction poses no significant problem for moisture

source: if the present Yarlung Tsangpo drainage system is able to persist in the lee of the high Himalayan orographic barrier, it is reasonable that at least as much water was available to the suture zone during the late Oligocene-early Miocene time, when much of the southern half of the Himalaya, including the highest part of the range, had yet to develop (e.g., Hodges, 2000).

The palaeoenvironmental interpretation discussed above is similar to published interpretations of Indus Group sedimentary rocks in the India-Asia suture zone of Ladakh, northern India (van Haver, 1984; Searle et al., 1990; Sinclair & Jaffey, 2001; Henderson et al., 2010). Although the Indus Group is not well dated, available information suggests its upper part is early Miocene (Sinclair & Jaffey, 2001). The Indus Group contains facies similar to those of the Kailas Formation, including coal, organic-rich shale, lacustrine deltaic and turbiditic deposits, and fringing coarse-grained fluvial-alluvial facies.

### **Basin Forming Mechanisms**

Potential causes of Kailas basin subsidence and low elevation include localized extension along the southern fringe of the Asian plate (DeCelles et al., 2011), or localized thrust loading in response to shortening in the Great Counter thrust system (Wang et al., 2015). The latter mechanism is not supported by the following aspects of the Kailas basin fill: (1) Sandstone petrographic data from the basin show that it has a magmatic arc provenance, quite unlike typical foreland basin sandstones, and not what would be expected if the sandstones were derived from the hanging wall of the Great Counter thrust; (2) consistent with (1), palaeocurrent data and conglomerate clast compositions indicate

that the Kailas Formation was derived predominantly from the north, rather than from an uplifted fold-thrust belt source to the south; (3) lithofacies along both southern and northern flanks of Kailas basin indicate close proximity to sediment sources, requiring that the present outcrop pattern closely approximates original basin width. In turn, this means that the Kailas basin was never more than about 20 km wide, which is not consistent with reasonable modeling that suggests a flexural foredeep basin would have had a much longer wavelength than the width of Kailas basin. And finally, (4) cross-cutting relationships and the absence of contractional growth structures in the Kailas Formation indicate that the Great Counter Thrust post-dates the Kailas Formation, which invalidates the interpretation that it could have supplied the flexural load to create the Kailas basin (Wang et al., 2015). Although Wang et al. (2015) illustrated examples of what they interpreted as growth structures in the Kailas Formation (their Supplementary Information Figures SI1-4b and SI1-8a, b), in all instances the growth strata are fanning southward, away from the Gangdese arc, which is inconsistent with development in response to Great Counter Thrust deformation, but supports our interpretation that the Kailas Formation was deposited in the hanging wall of a north-dipping normal fault system located along the southern basin flank (Fig. 8) (Leary et al., 2016).

It is also plausible that in its type area of the Kailas Range, the Kailas Basin could have formed by transtensional processes near the tip of the southeastward propagating Karakoram strike-slip fault system (Murphy et al., 2000). Available data suggest, however, that the Karakoram fault mostly postdates deposition of the Kailas Formation (Zhang et al., 2011), and several recent studies indicate that Karakoram fault slip is fed southeastward via the Gurla Mandata detachment fault into the thrust belt of central Nepal, rather than along

the Yarlung suture and the Kailas outcrop belt (Murphy et al., 2000, 2002; Murphy & Copeland, 2005; McCallister et al., 2014). Late Miocene apatite fission track ages from the Kailas Formation on the south flank of the Kailas Range were interpreted by Carrapa et al. (2014) as evidence for exhumation along an active strand of the Karakoram fault.

Part of the confusion regarding the origin of the Kailas basin stems from the fact that the Kailas Formation contains folds, minor faults, and vein arrays associated with the Great Counter thrust (e.g., Murphy & Yin, 2003; Wang et al., 2015), and the upper part of the unit contains abundant sedimentary clasts derived from Tethyan and ophiolitic source terranes to the south of the Great Counter Thrust. As noted above, the contractional structures in the Kailas Formation completely post-date its deposition. The Tethyan and suture zone sediment provenance is not diagnostic of tectonic setting in this case because these areas could have been uplifted in the footwall of a north-dipping normal fault or in the hanging wall of a thrust fault along the southern basin margin. To date, the best hard evidence for extension in the Kailas basin consists of extensional growth structures illustrated (and misinterpreted) by Wang et al. (2015), and evidence for local, large-magnitude extension ca. 26-18 Ma in the Ayi Shan (directly northwest of location 1 on Fig. 1a; Zhang et al., 2011). It is possible that extensional structures were eroded or structurally inverted during the transition from extension to shortening associated with the Great Counter thrust. Early Miocene extension in the Himalaya is widely known to be associated with the South Tibetan detachment (STD) fault system (e.g., Burg et al., 1984; Burchfiel et al., 1992). Although the extensional episode we infer for the Kailas basin was roughly synchronous with STD extension, it was restricted to the India-Asia suture zone some 40-100 km north of the trace of the STD, and is more closely related to north-side-down extension that has been



documented along the Indus suture zone in northern Pakistan (Treloar et al., 1991; Burg et al., 1996; Vince et al., 1996; Anczkiewicz et al., 1998, 2001) and in the nearby Ayi Shan (Zhang et al., 2011). Nevertheless, it is plausible that STD extension was geodynamically related to Kailas basin extension. New geochronological data from the Kailas Formation in the eastern part of its outcrop belt suggest that deposition continued there until ca. 18 Ma, and that in general the onset of sedimentation preceded local adakitic and ultrapotassic magmatism by several Ma (Leary et al., 2016a). Accordingly, it is likely that geodynamic processes responsible for the Kailas basin were spatially diachronous along the suture zone, from ca. 26 Ma in the west to 18 Ma in the east (Leary et al., 2016a).

Extension and crustal thinning in the upper plate of this rapidly colliding orogenic system can be explained by geodynamic models (e.g., Capitanio et al., 2010; Ueda et al., 2012) in which stresses transmitted via the mantle by slab rollback (or delamination) cause the trenchward part of the upper plate to extend, a process well-known in the Mediterranean region (e.g., Jolivet & Faccenna, 2000) but generally not considered for the India-Asia collision (but see Burg, 2011 for an exception). The buttress unconformity beneath the Kailas basin fill requires that the Gangdese arc was deeply eroded, presumably at moderate to high elevation, before Kailas deposition. This raises the prospect that even in extreme collisions, elevation gain may be punctuated by episodes of dynamic elevation loss (Saylor et al., 2009). The relatively undeformed character and very high present-day elevation of the Kailas Formation requires that sometime between the end of deposition (ca. 21-18 Ma, from west to east; Leary et al., 2016a) and today the basin experienced dramatic elevation gain. Thermochronological data indicate that the most likely time for elevation gain was ca.  $17 \pm 1$  Ma (Carrapa et al., 2014). In turn, this would suggest a coeval

return to northward underthrusting of the Indian plate, accompanied by shortening in the Great Counter Thrust system (Leary et al., 2016b) and restoration of regionally high elevation across the suture zone.

## CONCLUSIONS

Data presented here indicate that the Kailas basin contained large, deep, warm-water, probably meromictic lakes that likely formed at elevations thousands of meters lower than the modern 4500-6700 m elevations of Kailas Formation outcrops. These lakes filled with fine-grained, organic-rich profundal shale, progradational delta lobes (including Gilbert deltas), and deposits of various types of coarse- to fine-grained subaqueous sediment-gravity flows, including classic Bouma-type turbidites. Fringing the lake were coal-producing mires, fluvial systems, and basin-margin alluvial fans. The presence of a major erosional surface cutting into the plutonic core of the Gangdese magmatic arc beneath the Kailas Formation suggests that the basin substrate had already been uplifted and deeply eroded before basin formation. The strong contrast between Kailas Formation palaeolakes and coeval palaeolakes that developed in other areas of central Tibet, as well as modern high-elevation lakes in Tibet, demonstrates that the axis of the suture zone between India and Asia was, for ~5-7 Myr, depressed to low elevation relative to the surrounding Himalayan thrust belt and Tibetan Plateau. Geodynamic models attempting to explain the India-Asia collision process must incorporate a mechanism that will allow the southern fringe of the upper plate to be topographically depressed while collision continues. We rule out flexural subsidence because it does not produce features that are recorded in the Kailas basin. Transtensional strike-slip (but only locally near the southeastern end of the Karakoram fault)

or extension are more likely candidates. Shortening associated with the Great Counter Thrust overprinted the south flank of the Kailas basin, complicating the search for structural evidence of extension. Nevertheless, the stratigraphic features of the basin argue strongly for an extensional setting. Subsequently, the Kailas basin must have been topographically inverted, probably during the time period when thermochronological data indicate rapid cooling in response to incision and sediment evacuation (Carrapa et al., 2014).

#### **ACKNOWLEDGMENTS**

This research was funded by the National Science Foundation Continental Dynamics Program (EAR-1008527). Long-time collaborator Ding Lin helped with permits and logistics. We thank Kosuke Ueda, Paul Kapp, Andy Cohen, M.-M. Chang, Peter J. McCabe, and Jess Tierney for informative discussions and constructive suggestions. We thank George Gehrels, Mark Pecha and other staff members at the Arizona LaserChron Center for help with geochronological analyses. Jean-Pierre Burg and two anonymous reviewers provided comments and constructive criticisms to help us improve the manuscript. No conflict of interest is declared.

## REFERENCES CITED

- Akita, L.G. et al. (2015) Ostracoda (Crustacea) as indicators of subaqueous mass movements: An example from the large brackish lake Tangra Yumco on the southern Tibetan Plateau, China. *Palaeogeogr. Palaeoclimatol. Palaeoecol.* **419**, 60–74.
- Anczkiewicz, R., Burg, J.-P., Hussain, S.S., Dawood, H., Ghazanfar, M., & Chaudhry, M.N. (1998) Stratigraphy and structure of the Indus Suture Zone in the Lower Swat, Pakistan, NW Himalaya. *Jour. Asian Earth Sci.* **16**, 225-238.
- Anczkiewicz, R., Oberli, F., Burg, J.-P., Villa, I.M., Günther, D. & Meier, M. (2001) Timing of normal faulting along the Indus suture in Pakistan Himalaya and a case of major  $^{231}\text{Pa}/^{235}\text{U}$  initial disequilibrium in zircon. *Earth Planet. Sci. Lett.* **191**, 101-114.
- Bouma, A.H. (1962) Sedimentology of some Flysch deposits: A graphic approach to facies interpretation (Elsevier, Amsterdam).
- Bowen, G.J., & Wilkinson, B. (2002) Spatial distribution of  $\delta^{18}\text{O}$  in meteoric precipitation. *Geology*, **30**, 315–318.
- Buckles, L.K., Weijers, J.W.H., Verschuren, D. & Sinninghe Damsté, J.S. (2014) Sources of core and intact branched tetraether membrane lipids in the lacustrine environment: Anatomy of Lake Challa and its catchment, equatorial East Africa. *Geochim. Cosmochim. Acta* **140**, 106-126.
- Burchfiel, B. C., Chen, Z. L., Hodges, K. V., Liu, Y. P., Royden, L. H., Deng, C. R., & Xu, J. N., 1992, The south Tibetan detachment system, Himalayan orogen: Extension contemporaneous with and parallel to shortening in a collisional mountain belt. *Geol.*

*Soc. Amer. Spec. Paper* **269**, 41 pp.

Burg, J.-P. (2011) The Asia-Kohistan-India collision: Review and discussion. In Brown, D., & Ryan, P.D., eds., *Arc-Continent Collision*, 279-309, *Frontiers in Earth Sciences*, DOI 10.1007/978-3-540-88558-0-10. Springer-Verlag Berlin.

Burg, J.-P., Brunel, M., Gapais, D., Chen, G.M., & Liu, G.H. (1984) Deformation of leucogranites of the crystalline Main Central Sheet in southern Tibet (China). *Jour. Struct. Geol.* **6**, 535–542.

Burg, J.-P., Chaudhry, M.N., Ghazanfar, M., Anczkiewicz, R., & Spencer, D. (1996) Structural evidence for back sliding of the Kohistan Arc in the collisional system of Northwest Pakistan. *Geology* **24**, 739-742.

Capitanio, F. A., Stegman, D.R., Moresi, L., & Sharples, W. (2010) Upper plate controls on deep subduction, trench migrations and deformations at convergent margins, *Tectonophys.*, **483**, 80–92.

Carrapa, B. Orme, D.A., DeCelles, P.G., Kapp, P., Cosca, M.A. & Waldrup, R. (2014) Miocene burial and exhumation of the India-Asia collision zone in southern Tibet: response to slab dynamics and erosion. *Geology*, **42**, 443-446; doi:10.1130/G35350.1.

Castañeda, I.S. & Schouten, S. (2011) A review of molecular organic proxies for examining modern and ancient lacustrine environments. *Quat. Sci. Rev.* **30**, 2851-2891.

Chang, M., Wang, X., Liu, H., Miao, D., Zhao, Q., Wu, G., Liu, J., Li, Q., Sun, Z. & Wang, N. (2008) Extraordinarily thick-boned fish linked to the aridification of the Qaidam Basin (northern Tibetan Plateau). *Proc. Natl. Acad. Sci.* **105**, 13246-13251,

doi:10.1073/pnas.0805982105.

- Chen, G.-J. & Liu, J. (2007) First fossil barbin (Cyprinidae, Teleostei) from Oligocene of Qaidam Basin in northern Tibetan Plateau. *Vertebrata Palasiatica* **45**, 330-341.
- Chung, S.-L., Chu, M.-F., Zhang, Y., Xie, Y., Lo, C.-H., Lee, T.-Y., Lan, C.-Y., Li, X., Zhang, Q., Wang, Y. (2005) Tibetan tectonic evolution inferred from spatial and temporal variations in post-collisional magmatism. *Earth-Sci. Revs.*, **68**, 173–196.
- Cohen, A.S. (2003) Paleolimnology: History and Evolution of Lake Systems. Oxford Univ. Press, 500 pp.
- Colella, A. (1988) Fault-controlled marine Gilbert-type fan deltas. *Geology*, **16**, 1031-1034.
- Currie, B.S., Rowley, D.B. & Tabor, N.J. (2005) Middle Miocene palaeoaltimetry of southern Tibet; implications for the role of mantle thickening and delamination in the Himalayan Orogen. *Geology* **33**, 181-184.
- Currie, B.S., Polissar, P.J., Rowley, D.B., Ingalls, M., Li, S., Olack, G., & Freeman, K.H. (2016) Multiproxy paleoaltimetry of the late Oligocene-Pliocene Oiyug basin, southern Tibet. *Am. J. Sci.*, **316**, 401-436.
- DeCelles, P.G., Kapp, P., Gehrels, G.E. & Ding, L. (2014) Paleocene-Eocene foreland basin evolution in the Himalaya of southern Tibet and Nepal: Implications for the age of initial India-Asia collision. *Tectonics* **33**, doi:10.1002/2014TC003522.
- DeCelles, P.G., Kapp, P., Quade, J. & Gehrels, G.E. (2011) The Oligocene-Miocene Kailas Basin, southwestern Tibet: record of post-collisional upper plate extension in the Indus-Yarlung suture zone. *Geol. Soc. Am. Bull.* **123**, 1337-1362.

- DeCelles, P.G., Quade, J., Kapp, P., Fan, M., Dettman, D. & Ding, L. (2007) High and dry in the central Tibetan Plateau during the Oligocene. *Earth Planet. Sci. Lett.* **253**, 389-401.
- De Jonge, C., Hopmans, E.C., Zell, C.I., Kim, J.H., Schouten, S. and Damsté, J.S.S. (2014) Occurrence and abundance of 6-methyl branched glycerol dialkyl glycerol tetraethers in soils: Implications for palaeoclimate reconstruction. *Geochimica et Cosmochimica Acta* **141**, 97-112.
- Dewey, J.F., Shackleton, R.M., Chengfa, C. & Yiyin, S. (1988) The tectonic evolution of the Tibetan Plateau, *Philos. Trans. R. Soc. London, Ser. A*, **327**, 379-413.
- Dorsey, R.J., Umhoefer, P.J. & Renne, P.R. (1995) Rapid subsidence and stacked Gilbert-type fan deltas, Pliocene Loreto basin, Baja California Sur, Mexico. *Sediment. Geol.*, **98**, 181-204.
- Gansser, A. (1964) *Geology of the Himalayas* (London, Interscience), 289 p.
- Garzanti, E., Baud, A. & Mascle, G., (1987) Sedimentary record of the northward flight of India and its collision with Eurasia (Ladakh Himalaya, India). *Geodin. Acta* **1**, 297-312.
- Garzione, C.N., Dettman, D.L., Quade, J., DeCelles, P.G. & Butler, R.F. (2000) High times on the Tibetan Plateau: paleoelevation of the Thakkhola graben, Nepal. *Geology* **28**, 339-342.
- Gawthorpe, R.L. & Leeder, M.R. (2000) Tectono-sedimentary evolution of active extensional basins. *Basin Res.* **12**. 195-218.
- Gehrels, G.E., Valencia, V.A. & Ruiz, J. (2008) Enhanced precision, accuracy, efficiency, and spatial resolution of U- Pb ages by laser ablation- multicollector- inductively coupled plasma- mass spectrometry. *Geochem. Geophys. Geosyst.*, **9**, Q03017, doi:10.1029/2007GC001805.

Henderson, A.L., Najman, Y., Parrish, R., BouDagher- Fadel, M., Barford, D., Garzanti, E. &

Andò, S. (2010) Geology of the Cenozoic Indus Basin sedimentary rocks:

Paleoenvironmental interpretation of sedimentation from the western Himalaya during the early phases of India- Eurasia collision. *Tectonics*, **29**, TC6015, doi:10.1029/2009TC002651.

Hodges, K.V. (2000) Tectonics of the Himalaya and southern Tibet from two perspectives. *Geol. Soc. Amer. Bull.* **112**, 324–350.

Hoke, G.D., Liu-Zeng, J., Hren, M.T., Wissink, G.K. & Garzione, C.N. (2014) Stable isotopes reveal high southeast Tibetan Plateau margin since the Paleogene. *Earth Planet. Sci. Lett.* **394**, 270-278.

Hopmans, E.C., Schouten, S., Pancost, R.D., van der Meer, M.T.J. & Sinninghe Damsté, J.S. (2000) Analysis of intact tetraether lipids in archaeal cell material and sediments by high performance liquid chromatography/atmospheric pressure chemical ionization mass spectrometry. *Rapid Commun. MassSpectrom.* **14**, 585–589.

Hopmans, E.C., Weijers, J.W.H., Schefuß, E., Herfort, L., Sinninghe Damsté, J.S. & Schouten, S. (2004) A novel proxy for terrestrial organic matter in sediments based on branched and isoprenoid tetraether lipids. *Earth Planet. Sci. Lett.* **224**, 107–116, doi:10.1016/j.epsl.2004.05.012.

Hopmans, E.C., Schouten, S. and Damsté, J.S.S. (2016) The effect of improved chromatography on GDGT-based palaeoproxies. *Org. Geochem.* **93**, 1-6.

Hu, X., Garzanti, E., Moore, T. & Raffi, I. (2015) Direct stratigraphic dating of India Asia collision onset at the Selandian (middle Paleocene,  $59 \pm 1$  Ma). *Geology*, **43**, 859-862.



Huntington, K.W., Saylor, J., Quade, J. & Hudson, A.M. (2015) High late Miocene–Pliocene elevation of the Zhada Basin, southwestern Tibetan Plateau, from carbonate clumped isotope thermometry. *Geol. Soc. Am. Bull.* **127**, doi:10.1130/B31000.1.

Johnson, T.C., Wells, J.D., & Scholz, C.A. (1995) Deltaic sedimentation in a modern rift lake. *Geol. Soc. Am. Bull.*, **107**, 812-829.

Jolivet, L. & Faccenna, C. (2000) Mediterranean extension and the Africa-Eurasia collision. *Tectonics* **19**, 1095-1106.

Kapp, J.L.D., Harrison, T.M., Kapp, P., Grove, M., Lovera, O.M. & Ding, L. (2005) The Nyainqentanglha Shan: A window into the tectonic, thermal, and geo- chemical evolution of the Lhasa block, southern Tibet. *J. Geophys. Res.* **110**, B08413, doi: 10.1029/2004JB003330.

Kapp, P., Murphy, M.A., Yin, A. & Harrison, T.M. (2003) Mesozoic and Cenozoic tectonic evolution of the Shiquanhe area of western Tibet. *Tectonics*, **22**, 1029, doi:10.1029/2001TC001332.

Kim, J.H., van der Meer, J., Schouten, S., Helmke, P., Willmott, V., Sangiorgi, F., Koc, N., Hopmans, E.C. & Sinninghe Damsté, J.S. (2010) New indices and calibrations derived from the distribution of crenarchaeal isoprenoid tetraether lipids: implications for past sea surface temperature reconstructions. *Geochim. Cosmochim. Acta* **74**, 4639-4654.

Kropáček, J., Maussion, F., Chen, F., Hoerz, S. & Hochschild, V. (2013) Analysis of ice phenology of lakes on the Tibetan Plateau from MODIS data. *The Cryosphere* **7**, 287-301, doi:10.5194/tc-7-287-2013.

Lambiase, J.J. (1990) A model for the tectonic control of lacustrine stratigraphic sequences in continental rift basins, in Katz, B.J., ed., Lacustrine exploration: Case studies and modern analogues: *Amer. Assoc. Petrol. Geol. Mem.* **50**, 265–276.

Large, D.J., Spiro, B., Ferrat, M., Shopland, M., Kylander, M., Gallagher, K., Li, X., Chengde, S., Shen, C., Possnert, G., Zhang, G., Darling, W., & Weiss, D. (2009) The influence of climate, hydrology, and permafrost on Holocene peat accumulation at 3500m on the Eastern Qinghai–Tibetan Plateau. *Quat. Sci. Rev.* **28**, 3303–3314.

Lear, C.H., Elderfield, H., & Wilson, P.A. (2000) Cenozoic deep-sea temperatures and global ice volumes from Mg/Ca in benthic foraminiferal calcite. *Science* **287**, 269–272.

Leary, R.J., Orme, D.A., Laskowski, A., Peter G. DeCelles, Paul Kapp, Barbara Carrapa, B., and Dettinger, M., 2016a, Along-strike diachroneity in deposition of the Kailas Formation in central southern Tibet: Implications for Indian slab dynamics. *Geosphere*, in press.

Leary, R.J., DeCelles, P.G., Quade, J., Gehrels, G.E., and Waanders, G., 2016b, The Liuqu Conglomerate, southern Tibet: early Miocene basin development related to deformation within the Great Counter Thrust system. *Lithosphere*, in press.

Leier, A., DeCelles, P.G. & Kapp, P. (2007a) The Takena Formation of the Lhasa terrane, southern Tibet: the record of a Late Cretaceous retroarc foreland basin. *Geol. Soc. Am. Bull.*, **119**, 31–48.

Leier, A.L., DeCelles, P.G., Kapp, P. & Gehrels, G.E. (2007b) Lower Cretaceous strata of central Tibet: implications for regional deformation and uplift prior to the Indo-Asian collision. *J. Sed. Res.*, **77**, 809–825.

- Lippert, P.C., van Hinsbergen, D.J.J., & Dupont-Nivet, G. (2014) Early Cretaceous to present latitude of the central proto- Tibetan Plateau: A paleomagnetic synthesis with implications for Cenozoic tectonics, paleogeography, and climate of Asia, Asia, *in* Nie, J., Horton, B.K., & Hoke, G.D., eds., Toward an Improved Understanding of Uplift Mechanisms and the Elevation History of the Tibetan Plateau: *Geol. Soc. Am. Spec. Pap.* **507**, 1–21, doi:10.1130/2014.2507(01).
- Liu, Z., Pagani, M., Zinniker, D., DeConto, R., Huber, M., Brinkhuis, H., Shah, S.R., Leckie, R.M. & Pearson, A. (2009) Global cooling during the Eocene-Oligocene climate transition. *Science* **323**, 1187-1190.
- Liu, W., Wang, H., Zhang, C.L., Liu, Z., & He, Y. (2013) Distribution of glycerol dialkyl glycerol tetraether lipids along an altitudinal transect on Mt. Xiangpi, NE Qinghai-Tibetan Plateau, China. *Org. Geochem.*, **57**, 76-83.
- Long, H., Haberzettl, T., Tsukamoto, S., Shen, J., Kasper, T., Daut, G., Zhu, L., Mäusbacher, R. & Frechen, M. (2014) Luminescence dating of lacustrine sediments from Tangra Yumco (southern Tibetan Plateau) using post-IR IRSL signals from polymineral grains. *Boreas*, 10.1111/bor.12096. ISSN 0300-9483.
- Loomis, S.E., Russell, J. M., Ladd, B., Street-Perrott, F. A. & Sinninghe Damsté, J.S. (2012) Calibration and application of the branched GDGT temperature proxy on East African lake sediments. *Earth Planet. Sci. Lett.* **357**, 277-288.
- Loomis, S.E., Russell, J.M., Heurreux, A.M., D’Andrea, W.J. & Sinninghe Damsté, J.S. (2014) Seasonal variability of branched glycerol dialkyl glycerol tetraethers (brGDGTs) in a temperate lake system. *Geochim. Cosmochim. Acta* **144**, 173-187.

Lowe, D.R. (1982) Sediment gravity flows; II, depositional models with special reference to deposits of high-density turbidity currents. *J. Sed. Petrol.* **52**, 279-297.

Maldonado Fonkén, M.S. (2014) An introduction to the bofedales of the Peruvian High Andes. *Mires and Peat*, **15**, 1–13. ISSN 1819-754X.

McCabe, P.J. (1984) Depositional environments of coal and coal-bearing strata. *Spec. Pub. Int. Assoc. Sediment.* **7**, 13-42.

McCallister, A., Taylor, M., Murphy, M., Styron, R., Stockli, D., & Kapp, P. (2014) Thermochronologic constraints on the Late Cenozoic exhumation history of Gurlha Mandata, southwest Tibet, *Tectonics*, **33**, doi:10.1002/2013TC003302.

Mügler, I., Gleixner, G., Günther, F., Mäusbacher, R., Daut, G., Schütt, B., Berking, J., Schwalb, A., Schwark, L., Xu, B., Yao, T., Zhu, L. & Yi, C. (2010) A multi-proxy approach to reconstruct hydrological changes and Holocene climate development of Nam Co, Central Tibet. *J. Paleolimnol.* **43**, 625–648.

Mulder T. & Alexander, J. (2001) The physical character of subaqueous sedimentary density flows and their deposits. *Sedimentology*, **48**, 269-299.

Murphy, M.A., Yin, A., Kapp, P., Harrison, T.M., Ding, L. & Guo, J. (2000) southward propagation of the Karakoram fault system, southwest Tibet: timing and magnitude of slip. *Geology*, **28**, 451-454.

Murphy, M. A., A. Yin, P. Kapp, T. M. Harrison, C. E. Manning, F. J. Ryerson, D. Lin, & G. Jinghui (2002) Structural evolution of the Gurla Mandhata detachment system, southwest Tibet: Implications for the eastward extent of the Karakoram fault system,

*Geol. Soc. Am. Bull.*, **114**, 428–447.

Murphy, M.A. & Yin, A. (2003) Structural evolution and sequence of thrusting in the Tethyan fold-thrust belt and Indus-Yalu suture zone, southwest Tibet, *Geol. Soc. Am. Bull.* **115**, 21-34.

Murphy, M. A., & Copeland, P. (2005) Transtensional deformation in the central Himalaya and its role in accommodating growth of the Himalayan orogen, *Tectonics*, **24**, TC4012, doi:10.1029/2004TC001659.

Mutti, E. (1992) Turbidite Sandstones (Azienda Generale Italiana Petroli) 275 p.

Nemec, W. & Steel, R.J. (1984) Alluvial and coastal conglomerates: Their significant features and some comments on gravelly mass-flow deposits, *Sedimentology of Gravels and Conglomerates*, Koster, E.H., Steel, R.J., Eds., *Can. Soc. Petrol. Geol.* **10**, 1–31.

Orme, D.A., Carrapa, B. & Kapp, P. (2014) Sedimentology, provenance and geochronology of the upper Cretaceous–lower Eocene western Xigaze forearc basin, southern Tibet. *Basin Res.*, **27**, 387-411.

Pearson, E., Juggins, J., Talbot, H., Weckstrom, J., Rosen, P., Ryves, D., Roberts, S. & Schmidt, R. (2011) A lacustrine GDGT-temperature calibration from the Scandinavian Arctic to Antarctic: Renewed potential for the application of GDGT-paleothermometry in lakes. *Geochim. Cosmochim. Acta* **75**, 6225-6238.

Peterse, F., van der Meer, J., Schouten, S., Weijers, J.W.H., Fierer, N & Jackson, R.B. (2012) Revised calibration of the MBT–CBT paleotemperature proxy based on branched tetraether membrane lipids in surface soils. *Geochim. Cosmochim. Acta* **96**, 215-229.

Powers, L.P. Werne, J.P., Vanderwoude, A.J., Sinninghe Damsté, J.S., Hopmans, E.C. &

Schouten, S. (2010) Applicability and calibration of the TEX<sub>86</sub> paleothermometer in lakes.

*Org. Geochem.* **41**, 404–413.

Quade, J. Eiler, J., Daëron, M. & Achyuthan, H. (2013) The clumped isotope geothermometer

in soil and paleo sol carbonate. *Geochim. Cosmochim. Acta* **105**, 92–107, doi:

10.1016/j.gca.2012.11.031.

Quade, J., Breeker, D.O., Daeron, M. & Eiler, J. (2011) The paleoaltimetry of Tibet: an isotopic

perspective. *Am. J. Sci.* **311**, 77-115.

Rowley, D.B. & Currie, B.S. (2006) Paleoaltimetry of the late Eocene to Miocene Lunpola

basin, central Tibet. *Nature* **439**, 677-681.

Savin, S.M., Abel, L., Barrera, E., Hodell, D., Kennett, J.P., Murphy, M., Keller, G., Killingley, J.,

& Vincent, E. (1985) The evolution of Miocene surface and near-surface marine

temperatures: oxygen isotope evidence. In *The Miocene Ocean: Paleoceanography and*

*Biogeography* (J.P. Kennett ed). *Geol. Soc. Am. Mem.* **163**, 49-72.

Saylor, J.E., Quade, J., Dettman, D., DeCelles, P.G. & Kapp, P. (2009) The late Miocene

through present paleoelevation history of southwestern Tibet. *Am. J. Sci.* **309**, 1-42.

Schärer, U., Xu, R.H. & Allègre, C.J. (1984) U-Pb geochronology of Gangdese (Transhimalaya)

plutonism in the Lhasa-Xigaze region, Tibet. *Earth Planet. Sci. Lett.*, **69**, 311–320; doi:

10.1016/0012-821X(84)90190-0.

Schlische, R.W. (1992) Structural and stratigraphic development of the Newark extensional

basin, eastern North America: Evidence for the growth of the basin and its bounding

structures: *Geol. Soc. Amer. Bull.* **104**, p. 1246–1263, doi: 10.1130/0016-

Schoon, P.L., de Kluijver, A., Middelburg, J.J., Downing, J.A., Sinninghe Damsté, J.S. &

Schouten, S. (2013) Influence of lake water pH and alkalinity on the distribution of core and intact polar branched glycerol dialkyl glycerol tetraethers (GDGTs) in lakes, *Org. Geochem.* **60**, 72-82.

Schouten, S., Hopmans, E.C., Schefuß, E. & Sinninghe Damsté, J.S. (2002) Distributional variations in marine crenarchaeotal membrane lipids: a new tool for reconstructing ancient sea water temperatures? *Earth Planet. Sci. Lett.* **204**, 265–274.

Schouten, S., Huguet, C., Hopmans, E.C., Kienhuis, M.V.M. & Sinninghe Damsté, J.S. (2007) Analytical methodology for TEX<sub>86</sub> paleothermometry by high-performance liquid chromatography/atmospheric pressure chemical ionization-mass spectrometry. *Anal. Chem.* **79**, 2940–2944, doi:10.1021/ac062339v.

Shackleton, N.J., & Kennett, J.P., 1975, Paleotemperature history of the Cenozoic and the initiation of the Antarctic glaciation: Oxygen and carbon isotope analyses in DSDP sites 277, 279, and 281, in Kennett, J.P., and Houtz, R., eds., *Init. Rep. Deep Sea Drilling Proj. Leg 29*, 743–955.

Sinclair, H. D., & Jaffey, N. (2001), Sedimentology of the Indus group, Ladakh, northern India: Implications for the timing of initiation of the palaeo- Indus River. *Jour. Geol. Soc. London*, **158**, 151–162, doi:10.1144/jgs.158.1.151.

Sun, Q., Chu, G., Liu, M., Xie, M., Li, S., Ling, Y., Wang, X., Shi, L., Jia, G. & Lü, H. (2011) Distributions and temperature dependence of branched glycerol dialkyl glycerol tetraethers in recent lacustrine sediments from China and Nepal. *J. Geophys. Res.* **116**,

- Talling, P.J., Masson, D.G., Sumner, E.J. & Malgesini, G. (2012) Subaqueous sediment density flows: depositional processes and deposit types. *Sedimentology* **59**, 1937-2003.
- Taylor, M., Yin, A., Ryerson, F.J., Kapp, P. & Ding, L. (2003) Conjugate strike-slip faulting along the Bangong-Nujiang suture zone accommodates coeval east-west extension and north-south shortening in the interior of the Tibetan Plateau. *Tectonics*, **22**, 1044, doi:10.1029/2002TC001361.
- Tierney, J.E. & Russell, J.M. (2009) Distributions of branched GDGTs in a tropical lake system: implications for lacustrine application of the MBT/CBT paleoproxy. *Org. Geochem.* **40**, 1032-1036.
- Tierney, J.E., Russell, J.M., Eggermont, H., Hopmans, E.C., Verschuren, D. & Sinninghe Damsté, J.S. (2010) Environmental controls on branched tetraether lipid distributions in tropical East African lake sediments. *Geochim. Cosmochim. Acta* **74**, 4902–4918.
- Treloar, P.J., Rex, D.C., & Williams, M.P. (1991) The role of erosion and extension in unroofing the Indian Plate thrust stack, Pakistan Himalaya. *Geol. Mag.* **128**, 465-478.
- Tsao, W. & Wu, H. (1962) An Investigation of the Fish Biology and Fishery Problems in Ganze-Apa Region of Western Szechwan Province. *Acta Hydrobiol. Sinica* 1962, **32**.
- Ueda, K., Gerya, T.V. & Burg, J.P. (2012) Delamination in collisional orogens: Thermomechanical modeling. *J. Geophys. Res.* **117**, doi:10.1029/2012JB009144.
- Van Haver, T. (1984) Etude Stratigraphique sedimentologique et structural d'un basin d'avant arc: exemple du basin de l'Indus, Ladakh, Himalaya. Ph.D. thesis, University of



Grenoble, France.

Vince, K.J. & Treloar, P.J. (1996) Miocene, north-vergent extensional displacements along the Main Mantle Thrust, NW Himalaya, Pakistan. *Jour. Geol. Soc. London*, **153**, 677-680.

Volkman, J. (2003) Sterols in microorganisms. *Appl. Microbiol. Biotech.* **60**, 495-506.

Walton, E.K. (1967) The sequence of internal structures in turbidites. *Scott. J. Geol.* **3**, 306-317.

Wang, E., Kamp, P.J.J., Xu, G., Hodges, K.V., Meng, K., Chen, L., Wang, G. & Luo, H. (2015) Flexural bending of southern Tibet in a retro foreland setting. *Sci. Reps.* **5**, 12076, DOI: 10.1038/srep12076.

Wang, J., Peng, P., Ma, Q. & Zhu, L. (2010) Modern limnological features of Tangra Yumco and Zhari Namco, Tibetan Plateau. *J. Lake Sci.* **4**, 629–632.

Wang, M., Hou, J. & Lei, Y. (2014) Classification of Tibetan lakes based on variations in seasonal lake water temperature. *Chin. Sci. Bull.* **59**, 4847-4855, DOI 10.1007/s11434-014-0588-8.

Wang, N. & Chang, M.M. (2010) Pliocene cyprinids (Cypriniformes, Teleostei) from Kunlun Pass Basin, northeastern Tibetan Plateau and their bearings on development of water system and uplift of the area. *Sci. China Earth Sci.* **53**, 485-500, doi:10.1007/s11430-010-0048-5.

Wang, N. & Wu, F. (2014) New Oligocene cyprinid in the central Tibetan Plateau documents the pre-uplift tropical lowlands. *Ichthy. Res.* **62**, 274-285, doi: 10.1007/s10228-014-0438-3.

Weijers, J.W.H., Schouten, S., van den Donker, J.C., Hopmans, E.C. & Sinninghe Damsté, J.S.

(2007) Environmental controls on bacterial tetraether membrane lipid distribution in soils. *Geochim. Cosmochim. Acta* **71**, 703–713.

Wu, F.-Y., Ji, W.-Q., Wang, J.-G., Liu, C.-Z., Chung, D.-L. & Clift, P.D. (2014) Zircon U–Pb and Hf isotopic constraints on the onset time of India-Asia collision. *Am J Sci.*, **314**, 548-579; doi:10.2475/02.2014.04.

Wu, Y. & Chen, Y. (1980) Fossil Cyprinid Fishes from the Late Tertiary of North Xizang, China. *Vertebrata Palasiatica* **18**, 8.

Wu, Y. & Wu, C. (1992) The Fishes of the Qinghai-Xizang Plateau (Sichuan Science Technology Publishing House).

Yang, L., Mayden, R.L., Sado, T., He, S., Saitoh, K. & Miya, M. (2010) Molecular phylogeny of the fishes traditionally referred to Cyprinini sensu stricto (Teleostei: Cypriniformes). *Zoologica Scripta* **39**, 527-550, doi:10.1111/j.1463-6409.2010. 00443.x.

Zachos, J.C., Stott, L.D., & Lohmann, K.C. (1994) Evolution of marine temperatures during the Paleogene. *Paleoceanography*, **9**, 353–387.

Zhang, G.G., Yao, T., Xie, H., Qin, J., Ye, Q., Dai, Y. & Guo, R. (2014) Estimating surface temperature changes of lakes in the Tibetan Plateau using MODIS LST data. *J. Geophys. Res. Atmos.* **119**, 8552–8567, doi:10.1002/2014JD021615.

Zhang, G.Q., Xie, H.J., Yao, T.D. & Kang, S.C. (2013) Water balance estimates of ten greatest lakes in China using ICESat and Landsat data. *Chin. Sci. Bull.* **58**, 3815–3829, doi: 10.1007/ s11434-013-5818-y.

Zhang, R., Murphy, M.A., Lapen, T.J., Sanchez, V. & Heizler, M. (2011) Late Eocene crustal thickening followed by Early-Late Oligocene Extension along the India-Asia suture zone: Evidence for cyclicity in the Himalayan orogen. *Geosphere* **7**, 1249-1268; doi: 10.1130/GES00643.1.

Zhuang, G., Brandon, M.T., Pagani, M. & Krishnan, S. (2014) Leaf wax stable isotopes from Northern Tibetan Plateau: Implications for uplift and climate since 15 Ma. *Earth Planet. Sci. Lett.* **390**, 186–198.

Zink, K.-G., Vandergoes, M.J., Mangelsdorf, K., Dieenbacher-Krall, A.C. & Schwark, L. (2010) Application of bacterial glycerol dialkyl glycerol tetraethers (GDGTs) to develop modern and past temperature estimates from New Zealand lakes. *Organ. Geochem.* **41**, 1060-1066.

## Figure Captions

Fig. 1. (a) Digital topography of the southern Tibetan Plateau and central part of the Himalayan thrust belt, showing the Main frontal thrust (barbed line), major normal faults (ticked lines), Bangong suture zone (light dashed line), Great Counter thrust (GCT-heavy dashed line), and Karakoram strike-slip fault (opposing half-arrows), as well as geological rock units relevant to this paper (after Kapp et al., 2003 and Taylor et al., 2003). Modern large lakes are depicted in blue, including Tangri Yum Co (TY), Selin Co (S), and Nam Co (N). Numbered red circles are locations of stratigraphic sections of Kailas Formation referred to in the text and in Figures 2-5. Locations of Zhada basin (Z), Thakkhola basin (T), and Nima basin (NB) are shown. (b) Schematic cross-section showing the geological relationships of the synformal Kailas Formation to the Gangdese arc rocks (1), Great Counter Thrust (GCT)

and Xigaze forearc basin and associated ophiolitic rocks. Other numbered boxes indicate: (2) basal Kailas unconformity; (3) lower conglomerate member; (4) middle shale member; (5) basin center turbidite lobes; (6) upper sandstone/conglomerate member; and (7) coarse-grained basin-fringing deposits on south side of basin. Queried normal fault beneath GCT is hypothetical southern basin-bounding fault. Vertical scale of topography is ~2 km and vertical exaggeration is approximately 2.

Fig. 2. Logs of measured stratigraphic sections in Jiangzhu Valley (location 3, Fig. 1a) in southern and central part of the Kailas basin. See Table 1 for meanings of lithofacies codes. Boxed MDA refers to maximum depositional age based on detrital zircon U-Pb ages.

Fig. 3. Logs of measured stratigraphic sections in Yagra Valley (location 4, Fig. 1a). Diagram at right illustrates relative positions and correlations of the three separate sections. See Table 1 for meanings of lithofacies codes. Boxed MDA refers to maximum depositional age based on detrital zircon U-Pb ages.

Fig. 4. Log of measured stratigraphic section at location 1, Fig. 1. See Table 1 for meanings of lithofacies codes.

Fig. 5. Logs of measured stratigraphic sections of the lower Kailas conglomerate member and a portion of the middle shale member in the Linzhou Range (location 5, Fig. 1). See Table 1 for meanings of lithofacies codes. Boxed MDA refers to maximum depositional age based on detrital zircon U-Pb ages.

Fig. 6. Photographs of coarse-grained lithofacies in Kailas Formation. (a) Clast-rich subaqueous debris flow facies in section 3JV (see Fig. 2). Primary stratification dips toward left (south) at an angle of 70°. Hammer is 40 cm long. (b) Normally graded, but otherwise disorganized, bed of pebble to cobble conglomerate. Hammer is 40 cm long. (c) Megaforeset bedding in upper part of section 3JV (see Fig. 2). Master bedding is shown by solid lines, and clinoforms are indicated by dashed lines. Total thickness of the clinoform interval is approximately 30 m. (d) Disorganized, massive, subaerial debris flow facies in lower conglomerate member in the Linzhou Range (section LR, Fig. 5). Largest boulders are 1.5 m long.

Fig. 7. (a) View west of several-hundred-meter thick succession of distal lacustrine laminated black shale, with lenticular turbidite channel bodies (arrows) (see Fig. 4 for log of section 9KR). This is a typical section in the axial part of the Kailas basin. Low hill in lower left foreground conceals abandoned coal mine in lower part of the section. (b) Close-up view of laminated black shale. (c) Approximately 40 m thick succession of stacked Bouma-type sandy turbidite beds. Note tabular, laterally continuous bedding. (d) Normally graded, clast- and matrix-supported conglomerate with clasts streamlined parallel to palaeoflow direction (emphasized by white lines), characteristic of high-concentration, coarse-grained density flows. Hammerhead is 21 cm long. (e) Slump fold in sandy turbidite facies; hammer is 40 cm long. (f) Groove casts and prod marks on bottom of a sandy turbidite layer. (g) Flute casts on bottom of a Bouma-type sandy turbidite bed.

Fig. 8. Block diagram illustrating general depositional model for the Kailas basin in its type area of the Kailas Range, based on data presented in this paper combined with previous work (DeCelles et al., 2011). Kailas Magmatic complex is local name for rocks of the Gangdese arc. The Ayishan detachment fault and Gangdese arc basement are based on Zhang et al. (2011).

Fig. 9. Relative probability plots of detrital zircon U-Pb ages from Kailas Formation sandstone samples. Parenthetical numerals indicate mean ages of major peaks. Plots are normalized with respect to all grain ages in each sample such that areas beneath the probability curves are equal for all samples. Only the <200 Ma ages are shown for purposes of assessing maximum depositional ages. Values of n indicate the number of <200 Ma ages/total number of ages analyzed. Locations of samples are given in Figures 1a and 2-5.

Fig. 10. U-Pb zircon ages from Kailas Formation tuff samples. Uncertainties are reported at 2-sigma. MSWD is mean standard of weighted deviates. Locations of samples are given in Fig. 1a and Figs. 3-5.

Fig. 11. Cyprinidae gen. et sp. indet. from the Kailas Formation. (a) Nearly complete spine of dorsal fin, length 45 mm (IVPP V 20855.1); (b) nearly half vertebral centrum, each white or black dot indicating one annulus (IVPP V 20855.2); (c) incomplete pharyngeal bone with broken teeth (IVPP V 20855.3). Scale bar equals 10 mm in a, and 5 mm in b and c.

Fig. 12. HPLC chromatograms of the isoprenoid GDGT distribution of samples from (a) an early Holocene sample from the Bering Sea, (b) lacustrine Kailas Formation sample 1JV-110, and (c) marine surface sediments from offshore Mozambique in the southwestern Indian Ocean. The numbers 0-4 refer to the number of cyclopentane moieties in the GDGT structure. The GDGT with 4 cyclopentane moieties, crenarchaeol, has a regioisomer, which is indicated by 4'. TEX86 values range from 0 to 1 with higher values indicating higher temperatures. Applying the original calibration of Schouten et al. (2002), in which TEX86 values are calibrated to mean annual sea surface temperature, to all sites yields temperatures of 13°C, 27°C, and 34°C for the Bering, Kailas, and SW Indian Ocean samples, respectively. Applying the lacustrine TEX86 calibration to mean annual lake surface temperature (Peterse et al., 2012) to the Kailas sample yields a temperature of 30°C. Note that regardless of the calibration applied, the distribution of GDGTs in the Kailas Formation sample closely resembles that of the tropical SW Indian Ocean.

Table 1. Sample information for Kailas shales analyzed for organic geochemistry.

Sample ID*	Latitude	Longitude	~Elevation	Comments
1JV110	30.89285	81.67440	4960 m	GDGT's present
1JV25	30.89285	81.67440	4880 m	GDGT's present
6.18.12-1	31.25644	80.91882	5103 m	Thermally mature
6.18.12-2	31.25644	80.91882	5103 m	Thermally mature
9KR15	31.25891	80.91566	5150 m	Thermally mature
1JV184	30.89285	81.67440	5025 m	No detectable biomarkers
1JV256 <sup>†</sup>	30.89285	81.67440	5085 m	No detectable biomarkers
3JV221 <sup>†</sup>	30.6680	81.66177	5100 m	Trace isoprenoid & bGDGT's
LR100	29.90661	84.86103	5550 m	Trace isoprenoid & bGDGT's

\*With exception of samples 6.18.12-1 and 6.18.12-2, all samples are numbered according to section and meter level in the section.

<sup>†</sup>Sample contained trace amounts of isoprenoid and branched GDGTs but calculation of TEX<sub>86</sub> or MBT/CBT temperatures was not possible because one or more GDGTs were missing.



**Table 2.** Lithofacies (and their codes) used in logs of measured sections, and interpretations in this study.

Lithofacies Code	Description	Process Interpretation
<b>Fsl</b>	Laminated black or gray siltstone	Suspension-settling in ponds and lakes
<b>Fcl</b>	Laminated gray claystone	Suspension-settling in ponds and profundal lakes
<b>Fsm</b>	Massive, bioturbated, mottled siltstone, usually red; carbonate nodules common	Palaeosols, usually calcic or vertic
<b>Sm</b>	Massive medium- to fine-grained sandstone; bioturbated	Bioturbated sand, penecontemporaneous deformation
<b>Sr</b>	Fine- to medium-grained sandstone with small, asymmetric, 2D and 3D current ripples	Migration of small 2D and 3D ripples under weak (~20-40 cm/s), unidirectional flows in shallow channels
<b>St</b>	Medium- to very coarse-grained sandstone with trough cross-stratification	Migration of large 3D ripples (dunes) under moderately powerful (40-100 cm/s), unidirectional flows in large channels
<b>Sp</b>	Medium- to very coarse-grained sandstone with planar cross-stratification	Migration of large 2D ripples under moderately powerful (~40-60 cm/s), unidirectional channelized flows; migration of sandy transverse bars
<b>Sh</b>	Fine- to medium-grained sandstone with plane-parallel lamination	Upper plane bed conditions under unidirectional flows, either strong (>100 cm/s) or very shallow
<b>Srw</b>	Fine- to medium-grained sandstone with symmetrical small ripples	Deposition of oscillatory current (orbital) ripples in shallow lakes and ponds
<b>Gcm</b>	Pebble to boulder conglomerate, poorly sorted, clast-supported, unstratified, poorly organized	Deposition from sheetfloods and clast-rich debris flows
<b>Gcmi</b>	Pebble to cobble conglomerate, moderately sorted, clast-supported, unstratified, imbricated (long-axis transverse to palaeoflow)	Deposition by traction currents in unsteady fluvial flows
<b>Gch</b>	Pebble to cobble conglomerate, well sorted, clast-supported, horizontally stratified	Deposition from shallow traction currents in longitudinal bars and gravel sheets
<b>Gchi</b>	Pebble to cobble conglomerate, well sorted, clast-supported, horizontally stratified, imbricated (long-axis transverse to palaeoflow)	Deposition from shallow traction currents in longitudinal bars and gravel sheets
<b>Gct</b>	Pebble conglomerate, well sorted, clast-supported, trough cross-stratified	Deposition by large gravelly ripples under traction flows in relatively deep, stable fluvial channels
<b>Gcp</b>	Pebble to cobble conglomerate, well sorted, clast-supported, planar cross-stratified	Deposition by large straight-crested gravelly ripples under traction flows in shallow fluvial channels, gravel bars, and gravelly Gilbert deltas
<b>Gmm</b>	Massive, matrix-supported pebble to boulder conglomerate, poorly sorted, disorganized,	Deposition by cohesive mud-matrix debris flows or, in cases with sandy matrix, subaqueous debris flows

unstratified

<b>BB</b>	Single beds of boulders (up to 4 m in maximum dimension), unsorted, clast- or matrix-supported	Deposition by clast-rich or matrix-supported debris flows, followed by winnowing
<b>TBT</b>	Fine-grained sandstone in thinly interbedded sandstone-shale successions; planar basal surfaces, ripple cross-laminations and ripple forms	Thin-bedded turbidite facies. Distal fine-grained sandy turbidites (equivalent to Bouma Tc)
<b>S2</b>	Lowe S2 turbidite sandstone facies, comprising massive coarse-grained sandstone, locally normally and inversely graded, with dewatering structures	Deposition by high density turbidity currents or coarse-grained density flows
<b>Tabcd</b>	Bouma turbidite division a, b, c, and d; may be present as partial or complete sequences	Deposition by dilute sandy turbidity currents under hydrodynamically decelerating conditions

Table 3. Isoprenoid GDGT data from Kailas Formation samples, with calculated  $\text{TEX}_{86}$  values and derivative temperatures from marine (Schouten et al., 2002; Kim et al., 2010; Liu et al., 2009) and lacustrine (Powers et al., 2010; Castañeda et al., 2011; Tierney et al., 2010) calibrations. Note that the value reported from Kim et al. (2010) is calculated using the high temperature  $\text{TEX}_{86}^{\text{H}}$  calibration. BIT index values are calculated from Hopmans et al. (2004).

Sample	$\text{TEX}_{86}$	BIT Index	T°C Schouten et al. 2002	T°C Kim et al. 2010	T°C Liu et al. 2009	T°C Powers et al. 2010	T°C Castañeda et al. 2011	T°C Tierney et al. 2010
1JV110	0.804	0.723	34.4	32.1	30.2	30.4	28.4	27.7
1JV25	0.728	0.622	30.1	29.2	28.0	26.3	24.7	24.8

Table 4. Branched GDGT data from Kailas Formation samples, with calculated MBT/CBT (Weijers et al., 2007; Peterse et al., 2010; Pearson et al., 2011; Zink et al., 2010; Sun et al., 2011) and fractional abundance (Pearson et al., 2011; Tierney et al., 2010; Loomis et al., 2012) calibrations and derivative temperatures. MBT and CBT values are calculated following Weijers et al. (2007) and MBT' values following Peterse et al. (2010). Note that calibrations in Weijers et al. (2007) and Peterse et al. (2010) are based on soil samples whereas the others are based on lacustrine sediments.

Sample	BIT Index	MBT	MBT'	CBT	T°C Weijers et al. 2007	T°C Peterse et al. 2010	T°C Zink et al. 2010	T°C Sun et al. 2011	T°C Pearson et al. 2011	T°C Tierney et al. 2010	T°C Loomis et al. 2012
1JV110	0.710	0.651	0.663	0.150	25.0	19.9	32.5	29.9	19.4	35.7	19.5
1JV25	0.630	0.778	0.778	0.341	29.6	22.3	38.8	33.2	19.9	39.1	22.5

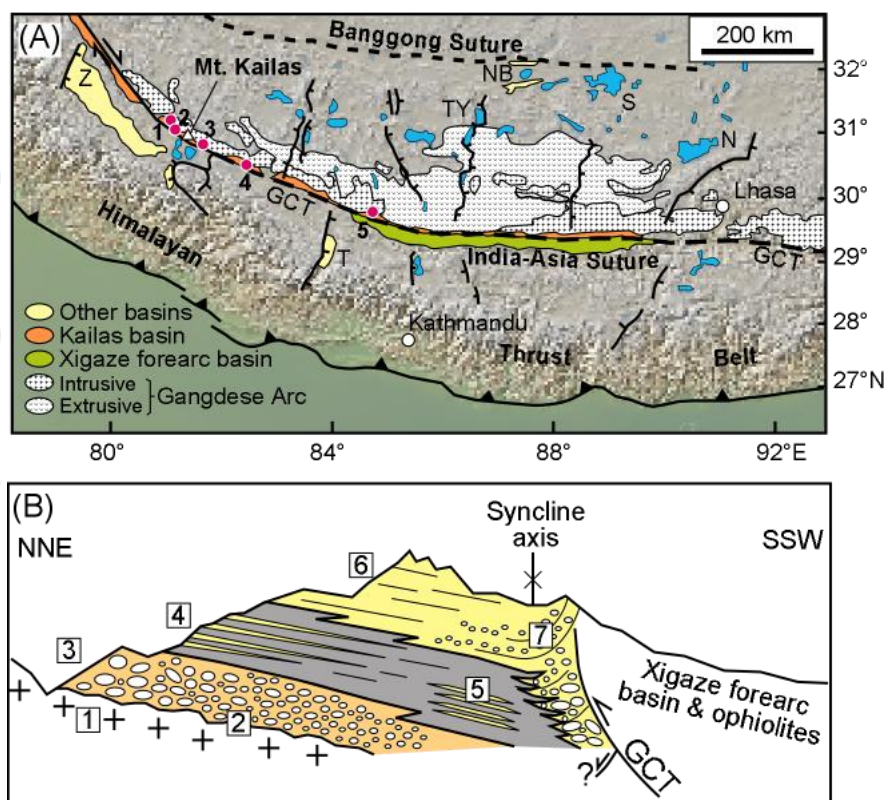


Fig. 1



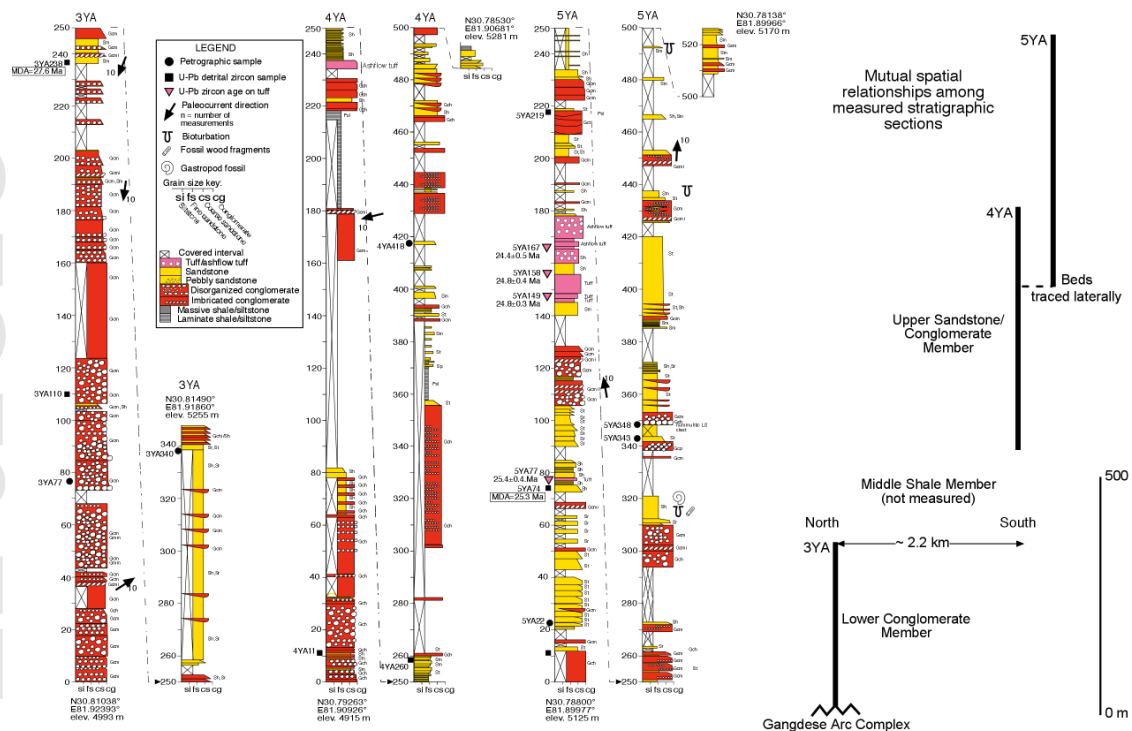


Fig. 3

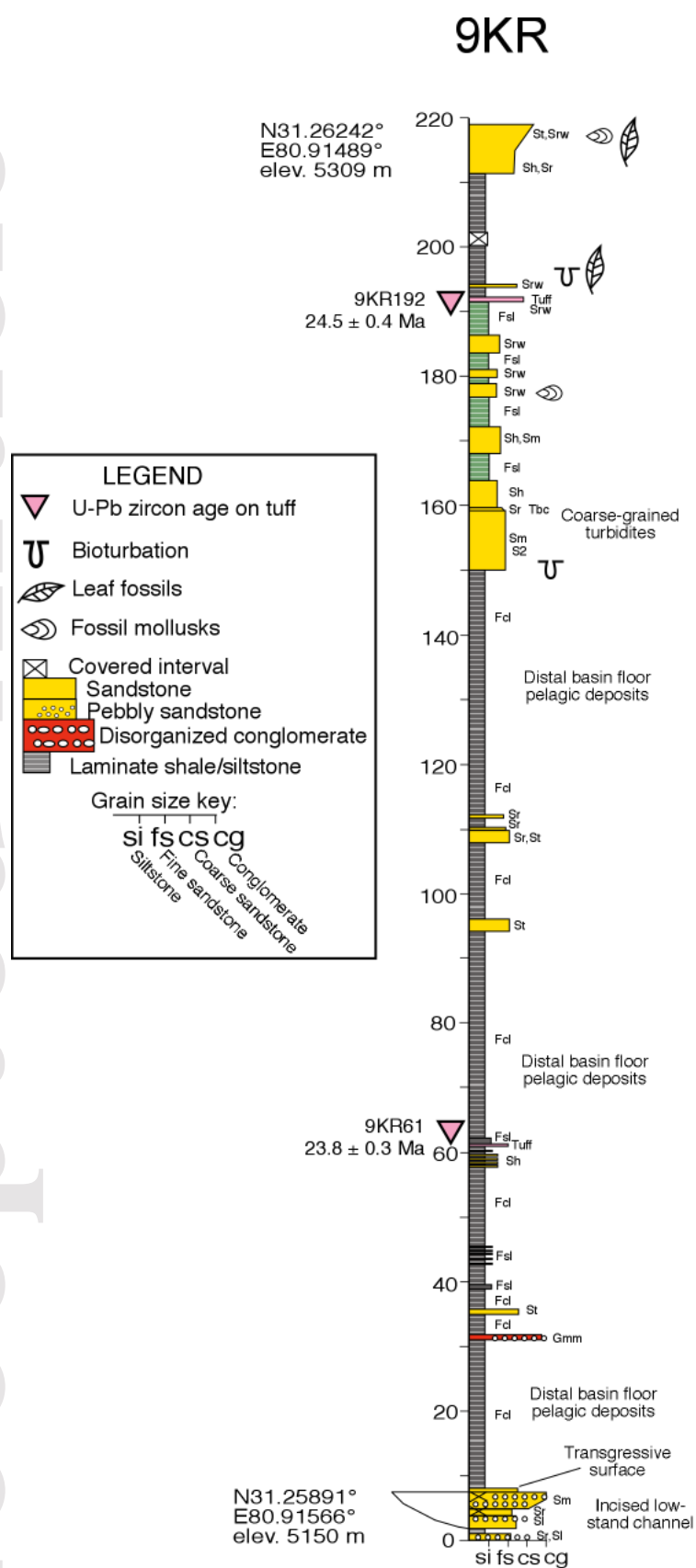
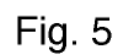
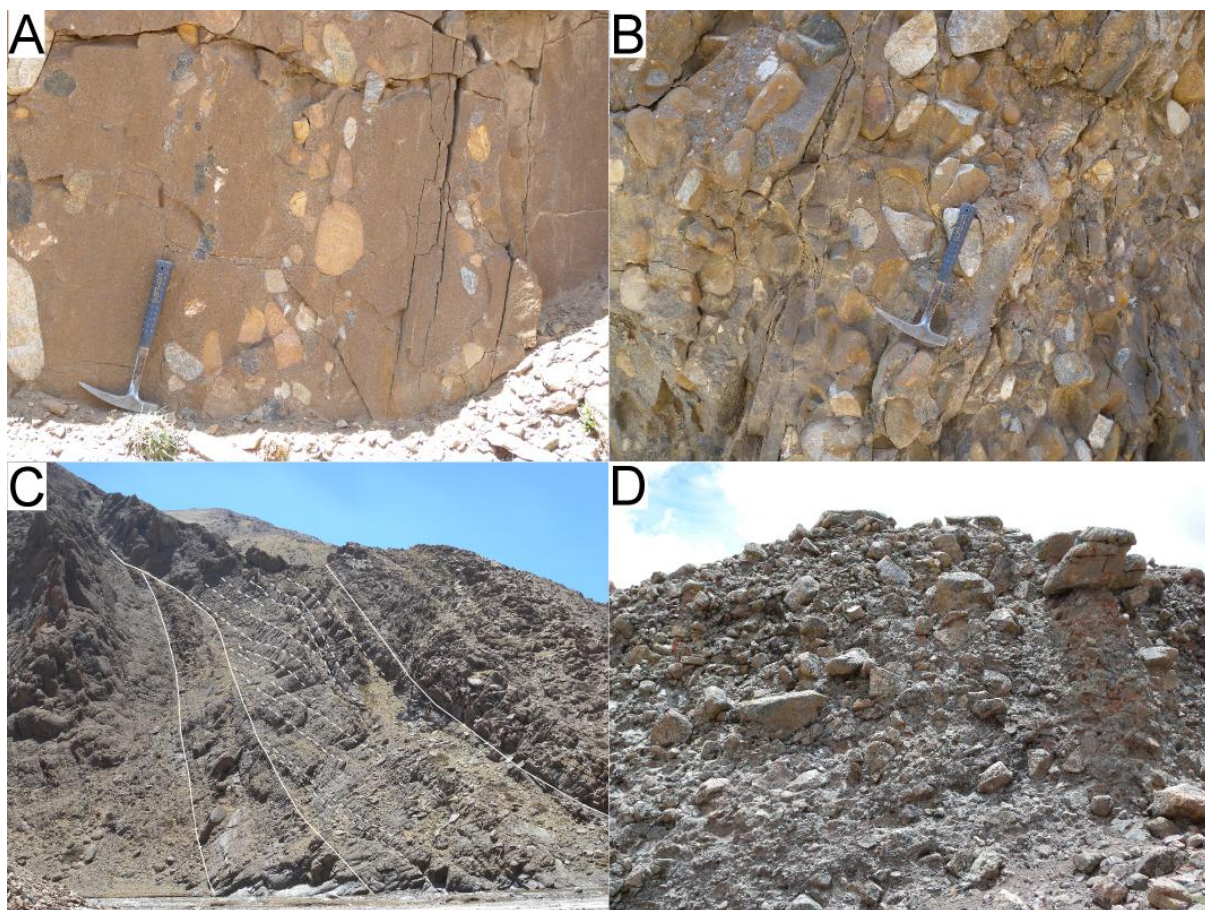


Fig. 4

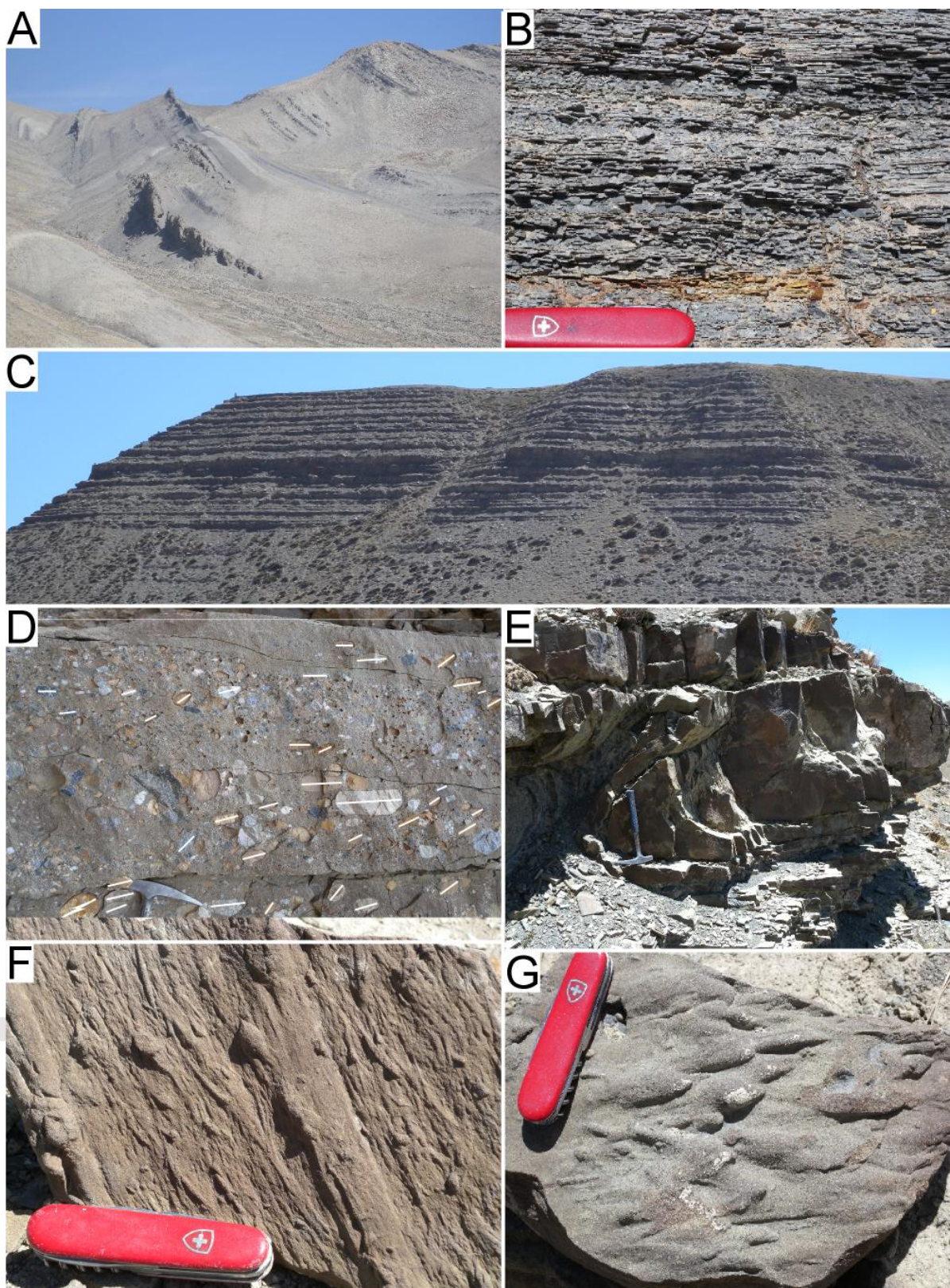


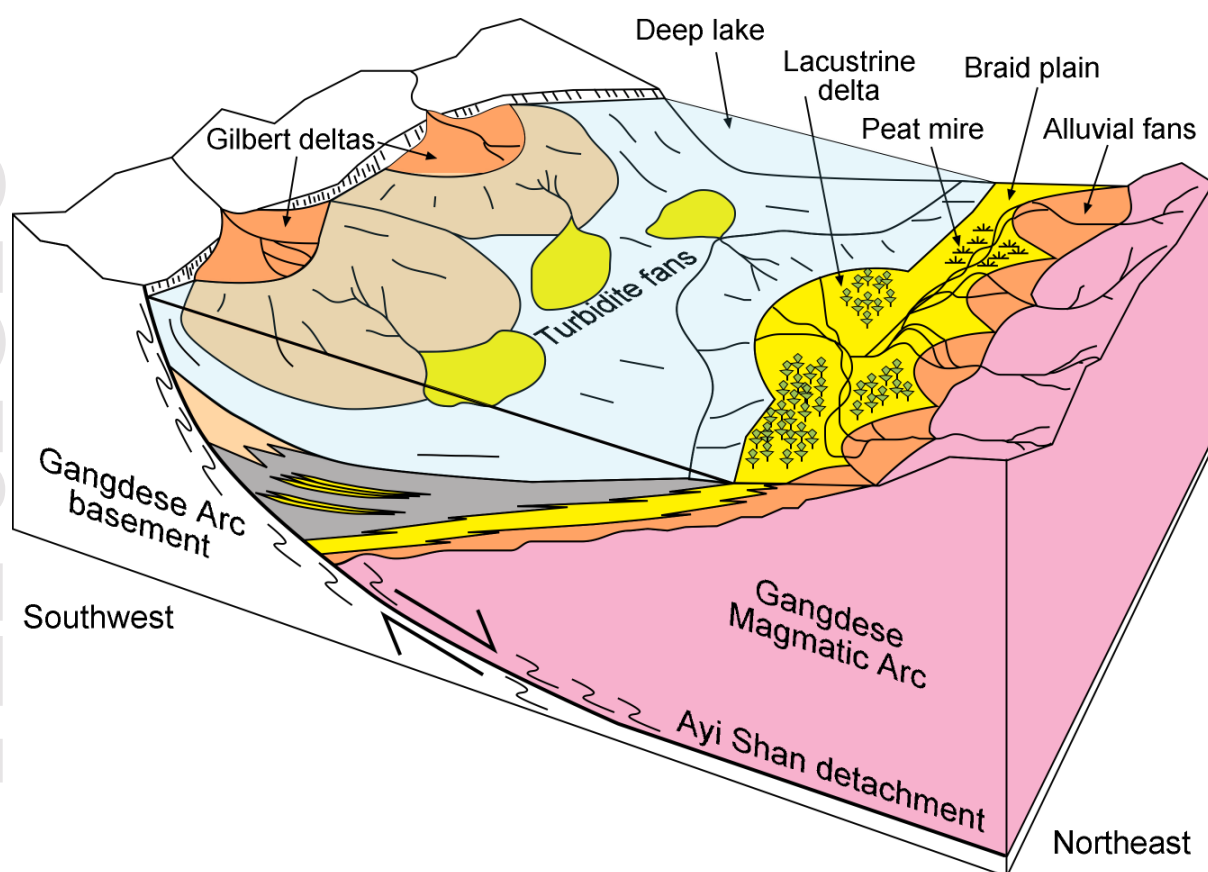














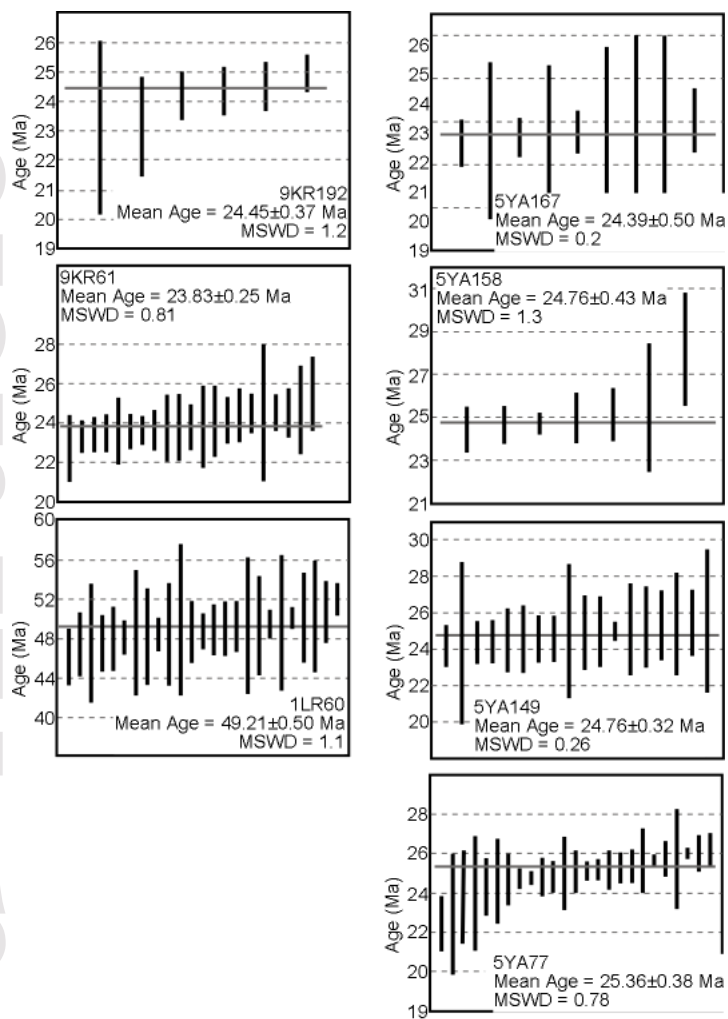


Fig. 9

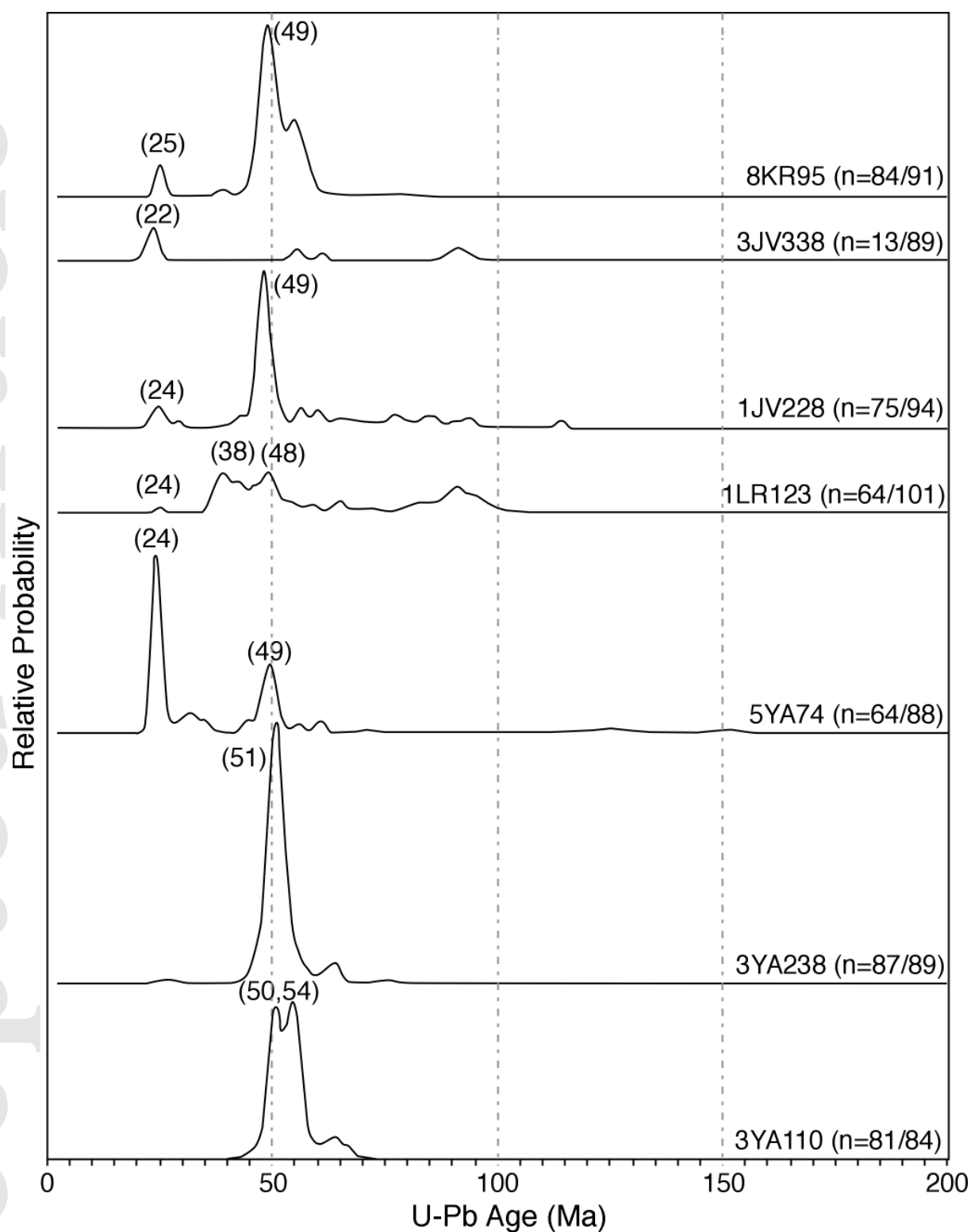
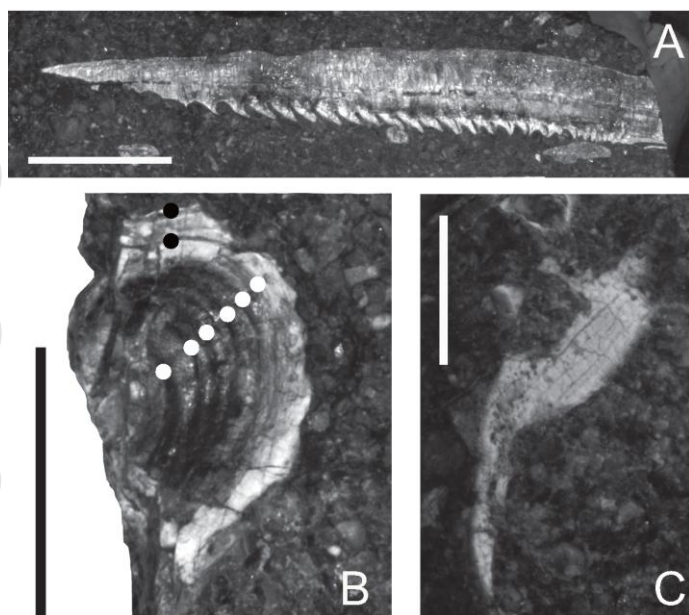


Fig. 10



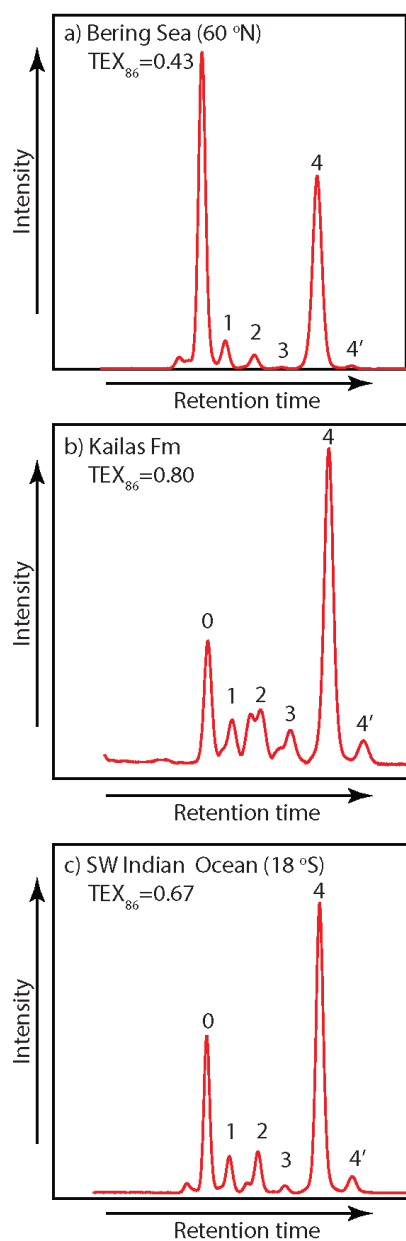


Fig. 12